

***A CASE STUDY OF HEAVY FOG MICROPHYSICAL STRUCTURE WITH A  
DROPLET SPECTROMETER***

Niu, S.,<sup>1\*</sup> Lu, C.,<sup>1,2</sup> Liu, Y.,<sup>2</sup> Zhao, L.,<sup>1</sup> Lv, J.,<sup>1</sup> and Yang, J.<sup>1</sup>

<sup>1</sup>Key Laboratory of Meteorological Disaster of Ministry of Education, School of Atmospheric Physics, Nanjing University of Information Science & Technology, Nanjing, China 210044

<sup>2</sup>Atmospheric Sciences Division, Brookhaven National Laboratory, Upton, NY 11973

\*Corresponding author: Prof. Shengjie Niu, Tel.: 02558731385; fax: (+86)2557792648; E-mail: niusj@nuist.edu.cn

Submitted for publication in  
*Advances in Atmos. Sci.*

December 2009

**Environmental Sciences Department/Atmospheric Sciences Division**

**Brookhaven National Laboratory**

P.O. Box 5000

Upton, NY 11973-5000

[www.bnl.gov](http://www.bnl.gov)

Notice: This manuscript has been authored by employees of Brookhaven Science Associates, LLC under Contract No. DE-AC02-98CH10886 with the U.S. Department of Energy. The publisher by accepting the manuscript for publication acknowledges that the United States Government retains a non-exclusive, paid-up, irrevocable, world-wide license to publish or reproduce the published form of this manuscript, or allow others to do so, for United States Government purposes.

This preprint is intended for publication in a journal or proceedings. Since changes may be made before publication, it may not be cited or reproduced without the author's permission.

## **DISCLAIMER**

This report was prepared as an account of work sponsored by an agency of the United States Government. Neither the United States Government nor any agency thereof, nor any of their employees, nor any of their contractors, subcontractors, or their employees, makes any warranty, express or implied, or assumes any legal liability or responsibility for the accuracy, completeness, or any third party's use or the results of such use of any information, apparatus, product, or process disclosed, or represents that its use would not infringe privately owned rights. Reference herein to any specific commercial product, process, or service by trade name, trademark, manufacturer, or otherwise, does not necessarily constitute or imply its endorsement, recommendation, or favoring by the United States Government or any agency thereof or its contractors or subcontractors. The views and opinions of authors expressed herein do not necessarily state or reflect those of the United States Government or any agency thereof.

## ABSTRACT

Examined are microphysical properties of a long-lasting heavy fog event from a comprehensive field campaign conducted during the winter of 2006 at Pancheng (32.2°N, 118.7°E), Jiangsu Province, China. It is found that the key microphysical properties (i.e., liquid water content, fog droplet concentration, mean radius and standard deviation) exhibit positive correlations with one another in general, and that the 5-min-average maximum value of fog liquid water content can be higher than 0.5 g m<sup>-3</sup>. Further analysis shows that the unique combination of positive correlations likely arise from simultaneous supplies of moist air and fog condensation nuclei associated with the advection of warm air, which further leads to high liquid water content. High values of liquid water content and droplet concentration conspire to cause low visibility < 50 m for a prolonged period of about 40 h. Examination of the microphysical relationships conditioned by the corresponding autoconversion threshold functions show that the collision-coalescence process likely occurs sometimes and weakens the positive correlations induced by droplet activation and condensational growth. Statistical analysis shows that the observed droplet size distribution can be well described by the Gamma distribution.

**Key words:** fog microphysics, positive correlation, high liquid water content, low visibility, warm and moist air

## 1. Introduction

Fog is a major natural hazard in many areas of the world, including China (Guo and Zheng, 2009; Niu et al., 2009). Studies have shown that the total economic losses associated with fog impacts on air, marine, land transportation can be comparable to those resulting from tornadoes, or, in some cases, winter storms and hurricanes (Gultepe et al., 2007). One of the most imperative fog factors is the low visibility induced by fog occurrence, and great effort has been devoted to developing fog models and parameterization of fog visibility in terms of fog microphysical properties. Early studies found that fog visibility is closely related to fog liquid water content ( $L$ ) (Eldridge, 1966, 1971; Tomasi et al., 1976; Pinnick et al., 1978; Kunkel, 1984). Recently, Gultepe and Milbrandt (2007) further introduced droplet concentration ( $N$ ) into the parameterization of visibility to account for the effect of varying  $N$  on visibility (Gultepe et al., 2001; Gultepe and Isaac, 2004).

Observational studies have been instrumental in our understanding of fog microphysics over the last few decades (Roach et al., 1976; Pinnick et al., 1978; Hudson, 1980; Gerber, 1981, 1991; Wendisch et al., 1998; Lu et al., 2008; Gultepe et al., 2009). Such studies have shown that fog layers are heterogeneous in nature (García-García et al. 2002), and exhibit dramatic variations in microphysical properties, with  $N$  changing up to two orders of magnitude (Gerber, 1981; 1991), and  $L$  from near-zero to  $0.5 \text{ g m}^{-3}$  (Fuzzi et al., 1992). Li (2001) summarized earlier observations in China and concluded that on average,  $N$  is increasingly higher for fogs occurring from coast areas to mountainous regions to city environment, while the behavior of mean fog droplet radius is just the opposite. This fog phenomenon appears to agree with what have been observed in warm clouds where an increase in aerosol concentration leads to an increase in cloud droplet concentration but a

decrease in mean droplet sizes (Twomey, 1977).

In spite of the considerable progress, the factors that affect fog microphysics are neither fully understood and nor properly parameterized in fog models, hindering fog forecasting/nowcasting (Croft et al., 1997; Gultepe et al., 2007). More observational studies with state-of-the-art instruments are needed. This is especially true in China where past observations of microphysical characteristics were largely based on gelatin-slide impactor systems. The temporal resolution of such systems is low, and less fog samples can be collected as result, prohibiting detailed investigation of fog microphysical characteristics.

Fog events occur rather frequently in Nanjing area of Jiangsu Province, China (Pu and Shen, 2001). To enhance our understanding of fog properties in this region, a comprehensive field campaign was carried out at Pancheng (32.2°N, 118.7°E), Jiangsu Province during the winter of 2006. Fog droplet size distributions were measured in sampling frequency of 1Hz with a FM-100 droplet spectrometer [Droplet Measurement Technologies (DMT)]. The spectrometer has been used and tested in many places worldwide (e.g. Eugster et al., 2006; Klemm and Wrzesinsky, 2007; Gultepe et al., 2009);but, this deployment was the first in China.

During the campaign, an exceptional deep fog event occurred from Dec. 24-27, 2006, with visibility lower than 50 m (sometimes only several meters) lasting for around 40 h. This heavy fog caused tremendous losses. For example, 8 automobiles piled up on a freeway in the northern Jiangsu Province with 7 people died and 5 injured; two ships collided with each other in the Yangtze river and one sank; the Nanjing Lukou International Airport was closed; the number of patients suffering from respiratory diseases increased considerably in hospitals.

This paper examines this disastrous fog event, with emphasis on the variability

and mutual relationships of key microphysical properties [ $L$ ,  $N$ , mean radius ( $\bar{r}$ ), and standard deviation ( $\sigma$ )]. The rest of the paper is organized as follows. Section 2 introduces the experiment site, instruments used for data collection, and the major approaches used to calculate key properties. Section 3 presents and discusses the results, including general characteristics of microphysics, fog droplet size distribution, microphysical relationships, and physical mechanisms for extremely high  $L$  and low visibility. Section 4 is the concluding remarks.

## **2. Experiment and method**

### ***2.1 Site description***

The field campaign was conducted from Nov. 30<sup>th</sup> to Dec. 27<sup>th</sup>, 2006, and the sampling site is located at Pancheng (32.2°N, 118.7°E; 22m a.s.l.), Jiangsu province, China. The site has several unique characteristics: located to the north of the Yangtze River and surrounded by various pollution sources (e.g., petrochemical factories, iron/steel works, and a thermal power plant).

### ***2.2 Instruments***

The measurements during the field campaign included fog droplet spectra, visibility, routine surface meteorological variables, and planetary boundary layer structure. As mentioned above, the size distributions of fog droplets were measured with a FM-100 droplet spectrometer (Gultepe and Milbrandt, 2007; Gultepe et al., 2009) (Figure 1). The instrument detects the number and size of individual fog droplets based on the forward light scattering by small particles. Particles scatter light from a laser diode of approximately 50 mW, and collecting optics guide the light from 5° to 14° into forward and masked (qualifier) detectors. The vacuum source pulls fog particles through a sample area at a known velocity, allowing particle concentrations

to be calculated. The intensity of the scattered light is then related to the droplet size. It measures fog droplets of 2 to 50  $\mu\text{m}$  in diameter, and can classify droplets up to 40 size classes. The calibration of the instrument was carried out by the manufacturer using glass beads of various sizes (7.8, 15.4, 19.9, 20.6, and 40.0 $\mu\text{m}$ ). The difference in optical properties of the glass beads as compared to water was taken into account in the calibration process. During this experiment, the instrument was set up 1m above the surface, and the mode with 20 size classes was selected.

Visibility was automatically measured and recorded every 15s by a ZQZ-DN visibility meter, a product of Radio Scientific Research Institute, Jiangsu Province, China. This instrument is designed according to *Guide to Meteorological Instruments and Methods of Observation (sixth edition)* from the World Meteorological Organization (WMO). Both the transmitter and receiver slope downwards for 13° and outwards for 10°, and the forward scattering angle is about 33°. In order to eliminate the influence of background light on the accuracy of visibility, the measurement system was modulated with rectangular wave. When the transmitter emits a near-infrared pulse of 930 nm wavelength with steady intensity, both the scattering energy from gas molecules, liquid and solid particles in the sampling volume and the energy of background light are collected by the receiver. When the transmitter is turned off, the receiver obtains only the energy of background light. The difference between these two pieces of received energy is the scattering energy from gas molecules and particles. With the difference value, visibility can be calculated. The relative error of the instrument is  $\pm 10\%$  /  $\pm 20\%$  when the visibility is less/greater than 1000 m.

Surface meteorological quantities (surface temperature, relative humidity, wind speed, and wind direction) were observed with an automatic weather station (EnviroStation™, ICT International Pty Ltd). All sensors have 16-bit resolution and

an accuracy of 1%-3%.

The Vaisala DigiCORA III tether sonde system was used to probe the planetary boundary layer (PBL). The measurements of temperature, pressure, humidity, wind speed and direction at various heights were delivered and saved in the computer and their vertical profiles were automatically displayed with vertical resolution 1-5 m. F-thermocap capacitive wire, H-humicap thin film capacitor, barocap silicon sensor, 3-cup anemometer, and digital compass were employed to measure temperature, humidity, pressure, wind speed, and wind direction, with resolutions 0.1 °C, 0.1%, 0.1 hPa, 0.1 m s<sup>-1</sup>, and 1°, respectively. In general, observations were performed every 3 h on fog-free days, and every 1-1.5 h on fog days if weather conditions (e.g., wind speed) permitted. The balloon was raised 600-1000 m high to meet the need of this fog research, and every observation lasted about 40 min.

### 2.3 Calculation method

According to *the Fog Monitor Operator Manual* provided by DMT, the true air speed ( $TAS$ , in unit of m s<sup>-1</sup>) of the spectrometer is calculated using the expression,

$$TAS = 20.06 \times M \times Ta^{0.5}, \quad (1)$$

where  $M$  is the Mach number derived from the dynamic (pitot) pressure and static pressure (in unit of millibars) (see Appendix A for details), and  $Ta$  is the actual ambient temperature (in unit of K). The sampling volume ( $V$ , in unit of cm<sup>3</sup> s<sup>-1</sup>) is calculated via the following equation,

$$V = TAS \times S, \quad (2)$$

where  $S = 0.264 \text{ mm}^2$  is the sampling area. The fog droplet counts divided by  $V$  provides  $n(r)$  in cm<sup>-3</sup> ( $r$  is the droplet radius).  $N$  (in unit of cm<sup>-3</sup>) and  $L$  (in unit of g m<sup>-3</sup>) of the whole spectra can be calculated as follows,

$$N = \sum n(r), \quad (3)$$



$$L = 1 \times 10^{-6} \times \rho \times \sum \frac{4\pi}{3} r^3 n(r), \quad (4)$$

respectively, where  $r$  (in unit of  $\mu\text{m}$ ) is the geometric average radius of every size interval, and  $\rho = 1 \text{ g cm}^{-3}$  is the density of water. In general, the p-order radius moment can be calculated with the following expression:

$$m_p = \int r^p \frac{n(r)}{N} dr = \sum r^p \frac{n(r)}{N} (p = 0, 1, 2, \dots). \quad (5)$$

In terms of the p-order radius moment,  $\bar{r}$  and  $\sigma$  are given by Eqs. (6) and (7), respectively:

$$\bar{r} = m_1, \quad (6)$$

$$\sigma = (m_2 - m_1^2)^{\frac{1}{2}}. \quad (7)$$

### 3. Results and discussions

#### 3.1 General characteristics

This fog began around 22:08 [all times are Beijing Standard Time (BST = UTC+0800) on Dec. 24<sup>th</sup>, 2006 and dissipated at 14:14 BST on Dec. 27<sup>th</sup>, lasting for more than 60 h. Visibility of less than 50 m occurred between 00:42 BST on the 25<sup>th</sup> and 13:00 BST on the 26<sup>th</sup>, and between 19:31 BST and 23:11 BST on the 26<sup>th</sup>, lasting for about 40 h (Figure 2a). It is noteworthy that the visibility was sometimes as low as only several meters. Fog events with such a low visibility and such a long duration occur rarely in this region.

Figures 2b-e further show the temporal variations of  $L$ ,  $N$ ,  $\bar{r}$ , and  $\sigma$ , respectively. It is clear from these figures that throughout the fog event, the microphysical properties all exhibit two primary oscillations and two secondary ones. Similar variation holds for the temporal evolution of the fog droplet spectra (Figure

3).

According to the variations of visibility and  $L$ , this fog event can be roughly divided into three stages: formation stage (from 22:08 BST, Dec. 24 to 00:35 BST, Dec. 25), development stage (from 00:35 BST, Dec.25 to 13:00 BST, Dec.26), and dissipation stage (from 13:00 BST, Dec.26 to 14:14 BST, Dec.27). The development stage is further composed of four periods: ascending period of the first  $L$  oscillation (from 00:35 BST, Dec. 25-02:45 BST, Dec. 25), descending period of the first  $L$  oscillation (02:45BST, Dec. 25-13:35 BST, Dec. 25), ascending period of the second  $L$  oscillation (13:35 BST, Dec. 25-00:18 BST, Dec. 26), and descending period of the second  $L$  oscillation (00:18 BST, Dec. 26-13:00 BST, Dec. 26). The major properties for each period are summarized in Table 1.

It is evident that with the exception of the peak radius, which remains largely unchanged at  $1.4\ \mu\text{m}$  during the whole event, the other microphysical quantities vary substantially. Similar fog characteristics were also reported in Huang et al. (2000). The mean  $N$  of this fog event is  $240.1\ \text{cm}^{-3}$ , only 15.8% of that in 1996 fog observed at the same site (Li, 2001). It is also lower than those observed in industrial cities, such as Chongqing ( $29.6\ ^\circ\text{N}$ ,  $106.5\ ^\circ\text{E}$ ), China (Li et al., 1992). On the other hand,  $N$  is comparable with that observed in Mengyang ( $22.1\ ^\circ\text{N}$ ,  $100.9\ ^\circ\text{E}$ ), Yunnan Province, and Chengdu ( $30.7\ ^\circ\text{N}$ ,  $104.1\ ^\circ\text{E}$ ), Sichuan Province, China (Li et al., 1992), and higher than that in Sierra Madre Oriental, Mexico (García-García et al., 2002), Waldstein, Germany (Klemm and Wrzesinsky, 2007), Pico del Este, Puerto Rico (Eugster et al., 2006). As to  $L$ , although the average is comparable with many other events, the 5-min-average maximum of this fog even exceeds  $0.5\ \text{g m}^{-3}$  (Figure 2b), while  $L$  has been usually lower than  $0.5\ \text{g m}^{-3}$  in previous campaigns (e.g. Li, 2001; Eugster et al., 2006; Beiderwieden et al., 2007).  $\bar{r}$ , peak radius ( $r_p$ ), and maximum

radius ( $r_{max}$ ) in this fog event are similar to those observed at Pancheng in 1996 (Li, 2001).

### ***3.2. Analytical expression for fog droplet size distribution***

Over the last few decades, great effort has been devoted to finding the appropriate analytical expression for describing the droplet size distribution because of its wide utilities in many areas. The Gamma function has been commonly used to describe cloud/fog droplet size distributions (e.g., Costa et al., 2000; Hsieh et al., 2009) such that

$$n(r) = N_0 r^\mu e^{-\lambda r}, \quad (8)$$

where  $r$  and  $n(r)$  are the droplet radius and the number of droplets per unit volume per unit radius interval, respectively;  $N_0$ ,  $\lambda$ , and  $\mu$  are the intercept, slope, and shape parameters, respectively.

Most previous studies on analytical size distributions have been based on empirical curve-fittings to individual measured distributions. Since a droplet size distribution is the end results of many complex processes that they can be considered to be stochastic in nature such as collision and coalescence (Jaw, 1966), statistical approaches that are applicable to a large number of individual size distributions are more desirable. Liu (1992, 1993) proposed such a simple statistical method based on the relationship between the skewness and kurtosis of the raindrop size distribution to identify the statistical distribution pattern. Liu and Liu (1994) and Liu et al. (1995) further applied a similar approach to study aerosol and cloud droplet size distributions. Here we apply the Liu approach to investigate if the statistical pattern of the fog droplet size distribution follows the Gamma distribution, and if there are any pattern differences among the different stages and periods. Briefly, skewness ( $S$ ) and kurtosis ( $K$ ) are defined as

$$S = \frac{\int (r - \bar{r})^3 \frac{n(r)}{N} dr}{[\int (r - \bar{r})^2 \frac{n(r)}{N} dr]^{3/2}}, \quad (9a)$$

$$K = \frac{\int (r - \bar{r})^4 \frac{n(r)}{N} dr}{[\int (r - \bar{r})^2 \frac{n(r)}{N} dr]^2} - 3, \quad (9b)$$

where  $\bar{r}$  is the mean radius. In terms of the p-order radius moments, the above two equations can be rewritten:

$$S = \frac{m_3 - 3m_1m_2 + 2m_1^3}{(m_2 - m_1^2)^{\frac{3}{2}}}, \quad (10a)$$

$$K = \frac{m_4 - 4m_1m_3 + 6m_1^2m_2 - 3m_1^4}{(m_2 - m_1^2)^2} - 3. \quad (10b)$$

For the Gamma distribution given by Eq. (8), it can be shown that

$$S = \frac{2}{\sqrt{1 + \mu}}, \quad (11a)$$

$$K = \frac{6}{1 + \mu}. \quad (11b)$$

Equations (11a, b) indicate that  $S = 2$  and  $K = 6$  are for the exponential distribution with  $\mu = 0$ . With the classical exponential distribution as a reference, the skewness and kurtosis deviation coefficients ( $C_s$  and  $C_k$ ) are introduced such that

$$C_s = \frac{S^2}{4}, \quad (12a)$$

$$C_k = \frac{K}{6}. \quad (12b)$$

It is obvious that for the Gamma distribution, we have

$$C_s = C_k = \frac{1}{1 + \mu}. \quad (13)$$

In the  $C_s$ - $C_k$  diagram, each  $(C_s, C_k)$  pair represents an individual droplet size distribution; the general Gamma distribution with varying  $\mu$  satisfies the diagonally straight line.

It is evident from Figure 4 that the values of  $C_s$  and  $C_k$  from all the 5-min-average droplet spectra fall near the straight line, suggesting that fog droplet size distributions of the whole event can be well described by the Gamma distribution. For comparison, also shown in Figure 4 are the pairs of  $C_s$  and  $C_k$  derived from the average spectra during the whole fog event and different stages/periods displayed in Figure 5. Obviously, these averaged droplet size distributions follow the Gamma distribution ( $C_s = C_k$ ) as well.

### 3.3 Microphysical relationships

To understand the physical processes responsible for this unusual fog phenomenon, this section explores the mutual relationships between the key microphysical properties. Figure 6a shows the relationship of  $\bar{r}$  to  $N$  for the whole fog event. Noteworthy is the phenomenon that  $\bar{r}$  and  $N$  during the fog event are positively correlated with each other. This positive  $\bar{r}$ - $N$  correlation differs from many previous studies (Li et al. 1999b, Huang et al. 2000, and Tang et al. 2002), and runs against the conventional wisdom that more aerosols result in more droplets and smaller mean radius when  $L$  remains unchanged. However, the positive  $\bar{r}$ - $N$  correlation suggests concurrent increases of  $N$  and  $L$ , which is clearly demonstrated in Figure 6b. Droplet activation with subsequent condensational growth (deactivation via complete droplet evaporation) can lead to co-increases (co-decreases) of  $N$  and  $L$ . The collection (collision and coalescence) process can also alter  $N$  and  $L$  simultaneously; however, it likely induces a negative, rather than positive correlation between  $N$  and  $L$ . Therefore, the positive  $N$ - $L$  correlation is further indicative of the dominance of two contrasting

processes: droplet activation with subsequent condensational growth and/or droplet deactivation via some complete droplet evaporation.

To further dissect whether droplet deactivation via some complete droplet evaporation has a major role in determining the microphysics in this fog, we examined the relationship of  $\sigma$  to  $\bar{r}$ ,  $N$ , and  $L$  (Figures 7a, b, c). It is clear that  $\sigma$  is positively correlated with  $\bar{r}$ ,  $N$ , and  $L$  as well. Recognizing that droplet evaporation associated with the conventional entrainment-mixing processes (Liu et al. 2002) unlikely lead to the concurrent increases of  $\sigma$ ,  $\bar{r}$ ,  $N$ , and  $L$ , we speculate that the process of droplet deactivation and droplet evaporation in this fog, if occurred, are largely reversible to the process of droplet activation and condensational growth.

It is noteworthy that the dominance of droplet activation with subsequent condensational growth or reversible evaporation does not rule out the roles of other processes completely. For example, according to the researchers who made the measurements, drizzling sometimes occurred during this fog event (unfortunately, no direct measurements of drizzle-sized drops were made during this event), which suggests the action of the collection process. To examine the strength of the collection process in this fog event, we calculated the autoconversion threshold function ( $T$ ) proposed by Liu et al. (2005, 2006) (see Appendix B for details). A larger value of  $T$  indicates a stronger collection process, ranging from no action ( $T = 0$ ) to full action ( $T = 1$ ). The results (Figure 8) agree favorably with the observers' report that drizzling sometime occurred during the fog event. Moreover, during the fog event, 5-min-average values of  $T$  span a wide range, from 0 to 0.87, providing a great opportunity to examine the influence of the collection process on the microphysical relationships discussed above. For this purpose, we classify the dataset into three groups ( $0 \leq T \leq 0.2$ ,  $0.2 < T < 0.6$ , and  $0.6 \leq T \leq 1.0$ ), and contrasts the microphysical

relationships among the three groups (Figure 9). In general, a higher  $T$  tends to correspond to a weaker positive correlation, or even irrelevance, negative correlation between the microphysical properties. In other words, collection process tends to destroy the positive correlation, because some big droplets grow by collecting small ones and result in increases of  $\bar{r}$  and  $\sigma$ , but a decrease of  $N$ .

Moreover, it is anticipated that different microphysical processes act in different stages/periods with different combinations, and that the exact microphysical relationships are determined by the degree of balance of these processes. This complex nature is evident from Figures 10-14, which compares the microphysical relationships in different stages/periods that are discussed below.

During the formation and dissipation stages, the size distributions are relatively narrow (Figure 3). Although there are two short-period developments in the dissipation stage, the concentrations of big droplets with radius  $> 10\mu\text{m}$  are very low (Figure 15). Therefore in the formation stage and the ascending periods of the secondary  $L$  oscillations in dissipation stage, droplet activation and condensation should be dominant, leading to strong positive correlations. While in the descending periods of the secondary  $L$  oscillations, in addition to evaporation, turbulent mixing may also be a factor.

During the development stage, the droplet spectra are broad with large concentrations of big droplets (radius  $> 10\mu\text{m}$ ), indicating that the processes of collection are likely important (Figures 3, 15). If collection was the main microphysical process,  $\bar{r}$  and  $N$  would be negatively correlated with each other. However, during the second  $L$  oscillation, the correlation coefficients are positively high, which is closely related to droplet activation with subsequent condensational growth. In this period, southern wind above the temperature inversion is stronger than

those at the surface and adjacent layers, indicating more obvious warm advection above the inversion (Figure 16). As a result, the temperature above the inversion is always higher than the surface and adjacent layer even after sunrise, so the inversion is maintained stably. At the same time, the southerly moisture advection provides substantial water vapor which accumulates under the inversion. In addition to sufficient supply of moisture, considerable aerosol particles discharged from nearby industrial activities are accumulated. Based on Tong (2008), aerosol concentration at Pancheng is high and water soluble materials are major compositions of the aerosol particles, providing sufficient source of fog condensation nuclei in this area. As a result, the small droplets are reproduced through droplet activation with subsequent condensational growth promoted by sufficient supplies of water vapor and fog condensation nuclei. These new small droplets may compensate for the loss caused by collection. As a result, the evolution of small droplet number concentration is almost in phase with that of big ones (Figure 15).  $\bar{r}$  is mainly determined by big droplets while  $N$  is dominantly contributed by small ones. Therefore  $\bar{r}$  and  $N$  show positive correlation in the second  $L$  oscillation (Figure 10c), the concurrent variations of  $\sigma$ ,  $\bar{r}$ ,  $N$ , and  $L$  are also expected (Figures 11c, 12c, 13c, 14c). Unfortunately in the first  $L$  oscillation, we do not have the whole observations of boundary layer structure. But as seen from the high speed center above 200 m after 07:00 on the 25<sup>th</sup> (Figure 16a), it is believed that the warm and moist air exists in the whole first  $L$  oscillation. Different from the second  $L$  oscillation, the correlation coefficients of  $\bar{r}$  vs.  $N$  are relatively lower, but still positive (Figure 10b). In the ascending period of the first  $L$  oscillation, temperature decreases due to longwave radiation (Figure 2f), causing the development of activation and condensation. As a result, small droplets increase remarkably at 01:10 on the 25<sup>th</sup> (Figure 15). Then the broadening of spectra is very sudden from



01:10 to 02:45 on the 25<sup>th</sup> with a rapid increase of big droplets, indicating that the collection develops and consumes small droplets. As a result, small droplets decrease sharply from 01:10 to 02:45, and the positive correlation of  $\bar{r}$  and  $N$  in this period is not very significant. Similarly, the correlation coefficients of  $N$  vs.  $L$  and  $\sigma$  vs.  $N$  are lower (Figures 11b, 13b) but  $\sigma$  still has a good positive correlation with  $\bar{r}$  and  $L$  (Figures 12b, 14b). During the descending period of the first  $L$  oscillation, human activities after sunrise (06:55 BST) provide plenty of fog condensation nuclei, producing a large number of small droplets through droplet activation and condensation. As a result, during 08:42 BST-12:40 BST on the 25<sup>th</sup>, two obvious peaks of small droplet concentration are achieved (Figure 15). However, the peaks of big droplet concentration are weak, resulting in only small variation of  $\bar{r}$  (Figure 2d). Then positive correlation between  $N$  and  $\bar{r}$  is not that significant during the whole period (Figure 10b). Due to the very high positive correlation coefficient of  $\sigma$  and  $\bar{r}$  (Figure 12b), the variation of  $\sigma$  is expected to be similar to  $\bar{r}$  with small variation during 08:42 BST-12:40 BST. This might be the main reason for the poor correlation between  $\sigma$  and  $N$  (Figure 13b) in this period. In general, with the development of collection during the development stage, small droplets (radius  $\leq 10 \mu\text{m}$ ) with  $0.2 < T < 0.6$  are almost equal to those with  $0.6 \leq T \leq 1.0$  (Figure 17), suggesting that although the formation of big droplets (radius  $> 10 \mu\text{m}$ ) consumes small ones, the production of small ones through activation with subsequent condensational growth can compensate the loss caused by collection, which provides another evidence to support the conclusion that droplet activation with subsequent condensational growth is the predominant process.

### ***3.4 Physical reasons for high liquid water content and low visibility***

Another striking feature of this fog is its high maximum  $L$  and low visibility. As shown in Figure 2b, during the two nights of development stage,  $L$  reaches its 5-min-average maximum  $> 0.5 \text{ g m}^{-3}$ . And as mentioned above, visibility  $< 50 \text{ m}$  lasts for about 40 h with sometimes only several meters (Figure 2a). This section explores the physical reasons for the unusually high  $L$  and low visibility.

As shown above, in general, the key quantities of  $N$ ,  $L$ ,  $\sigma$ , and  $\bar{r}$  are positively correlated to one another during the whole event. The synchronous increase of  $N$ ,  $\sigma$ ,  $\bar{r}$  and  $L$  is the first microphysical reason for high  $L$ . Another reason is closely related to high fog top (200-600 m) (Figure 16c), which is higher than many fog events previously reported (Pilié et al., 1975; Roach et al., 1976; Guedalia and Bergot, 1994; Li et al., 1999a, b). Other things being equal, a higher top allows more time for droplets to grow larger, leading to a higher  $L$ , because gravitational settling of droplets in the upper layer of fog body can collect some droplets and cause the formation of bigger droplets and the increase of  $L$  in the surface and adjacent layer. The dependence of  $L$  on the fog thickness ( $H$ ) is quantified by a theoretical expression derived by Zhou and Ferrier (2008) for a steady-state fog:  $L \sim H^{1/2}$ . Although this expression is derived for radiation fog at the steady state and under uniform turbulence, it may also give us some hints to estimate  $L$ . For example, the value of  $L$  around 00:00 on the 26<sup>th</sup> calculated using this expression is  $0.6 \text{ g kg}^{-1}$ , very close to our observation (see Appendix C for details).

It is worth mentioning that high values of  $L$  have been also reported in other fogs observed in other places of the world. Gultepe et al. (2009) conducted three field campaigns of the Fog Remote Sensing And Modeling (FRAM) project over the following two regions of Canada: 1) the Center for Atmospheric Research

Experiments (CARE) near Egbert, Ontario (FRAM-C) and 2) Lunenburg, Nova Scotia (FRAM-L). FRAM-C took place during the period from November 2005 to April 2006, and FRAM-L1 and L2 occurred during June 2006 and June 2007, respectively. In their Figure 6c,  $L > 0.5 \text{ g m}^{-3}$  was also found. During 2000 and 2001/2002, a campaign was carried out in Waldstein, Germany with fog physics and chemistry measured. Using the same FM-100 spectrometer, it was found that many 5-min-average values exceeded  $0.5 \text{ g m}^{-3}$  (Wrzesinsky, 2003), which were also shown in Figure 2 and Table 1 of Klemm et al. (2005). Herckes et al. (2007) conducted an intensive observation in California's San Joaquin Valley during 2000/2001 and a Gerber Scientific Particulate Volume Monitor (PVM-100) was employed to measure  $L$ . Their Figure 1 showed that even in a very thin fog, high  $L$  was detected with some values over  $0.5 \text{ g m}^{-3}$ . They found that at times the drops became so large that the fog began to form what appeared to be drizzle, similar to the result in this work.

As discussed above,  $L$  and  $N$  show a good positive correlation. During the fog event, especially the two nights of development stage,  $L$  and  $N$  are high. The concurrent high values of  $L$  and  $N$  conspire to cause low visibility because visibility is inversely proportional to the product of  $L$  and  $N$  (Gultepe and Milbrandt, 2007).

#### **4. Concluding remarks**

An unusual fog event that occurred from 24<sup>th</sup> to 27<sup>th</sup> Dec. and had low visibility  $< 50 \text{ m}$  (sometimes only several meters) lasting for approximately 40 h was encountered and observed during a field campaign conducted during the winter of 2006. The measurements included fog droplet size distributions, visibility, common meteorological variables and planetary boundary layer structure. This paper focuses on the major microphysical properties and their mutual relationships. The fog droplet

size distributions are also examined.

It is found that throughout this whole fog event, fog droplet concentration, liquid water content, mean radius and standard deviation are positively correlated to one another in general. Further analysis reveals that the positive correlations likely arise from the dominance of droplet activation with subsequent condensational growth during this fog event. It is also found that the collection (collision and coalescence) process occurs with different degrees in different stages/periods. A stronger collection process is generally associated with weaker positive correlations, suggesting that the collection process tends to destroy some of the positive correlations, in agreement with theoretical expectation. The concurrent increases of droplet concentration, liquid water content, mean radius and standard deviation, together with high fog top, and gravitational settlement, further lead to high liquid water content and poor visibility. Statistical analysis also shows that the fog droplet size distributions, being 5-min or averaged during different stages/periods or the whole event, can all be well described by the Gamma distribution.

A few points are noteworthy in passing. First, our preliminary analysis indicates that a main macrophysical reason for these unique microphysical properties are a stable boundary structure under the influence of warm advection with sufficient supplies of both moisture and fog condensation nuclei. More detailed study of the macrophysics for this fog is underway and will be reported elsewhere. Second, the possibility of a positive  $\bar{r}$ - $N$  correlation was pointed out in 1965 by Hong and Huang (1965). Furthermore, there have been similar studies on clouds. For example, Hudson and Svensson (1995) analyzed the cloud microphysical properties off the southern California coast and found that  $\bar{r}$  and  $N$  showed negative correlations for most cases, but still in three cases the relationships were positive, which was caused by the cloud

condensation nuclei plume. Considering that fog is an extreme cloud near the surface, both similarities and differences between clouds and fogs are expected. A comprehensive investigation of fogs and clouds together would be desirable to improve our understanding and parameterization of fog and cloud microphysics.

***Acknowledgements.*** Funding for this work was mainly provided by the National Natural Science Foundation of China (Grant No. 40537034 and 40775012), Natural Science Fund for Universities in Jiangsu Province (Grant No. 06KJA17021), Meteorology Fund of Ministry of Science and Technology (Grant No. GYHY (QX) 2007-6-26) and Graduate Student Innovation Plan in Universities of Jiangsu Province (CX09B\_226Z). Yangang Liu was supported by the Atmospheric System Research (ASR) program of the U. S. Department of Energy. Dr. Binbin Zhou at NOAA Environmental Modeling Center provided valuable suggestions.

## Appendix A: Calculation of the Mach Number

The expression for calculating the Mach number is given by,

$$M = \left\{ 2 \times \frac{C_v}{R} \times \left[ \left( \frac{Q_c}{P_s} + 1 \right)^{\frac{R}{C_p}} - 1 \right] \right\}^{0.5}, \quad (\text{A1})$$

where  $C_v$ ,  $C_p$  and  $R$  are specific heat at constant volume, specific heat at constant pressure and gas constant for dry air, respectively. In addition,  $Q_c$  and  $P_s$  are dynamic (pitot) pressure and static pressure which can be converted from analog to digital value ( $AD_1$ ) of Sensor #1 and  $AD_2$  value of Sensor #2 in fog droplet spectrometer via

$$Q_c = 2.4884 \times \frac{20 \times \frac{AD_1}{4095} - 10}{5}, \quad (\text{A2})$$

and

$$P_s = 68.9476 \times 3 \times \left( 20 \times \frac{AD_2}{4095} - 10 - 1 \right), \quad (\text{A3})$$

respectively.

## Appendix B: Autoconversion Threshold Function

According to Liu et al. (2005, 2006), all the autoconversion parameterizations that have been developed so far can be generically written as

$$P = P_0 T, \quad (\text{B1})$$

where  $P$  is the autoconversion rate,  $P_0$  is the rate function describing the conversion rate after the onset of the autoconversion process, and  $T$  is the threshold function describing the threshold behavior of the autoconversion process. Size truncation function employed to quantify the effect of truncating the cloud droplet size distribution on the autoconversion rate can be used as a threshold function to represent the threshold behavior associated with the autoconversion process, providing a physical basis for the threshold function. The expression of  $T$  can be

generally described by

$$T = \frac{P}{P_0} = \frac{\left[ \frac{\int_{r_c}^{\infty} r^6 n(r) dr}{\int_0^{\infty} r^6 n(r) dr} \right]}{\left[ \frac{\int_{r_c}^{\infty} r^3 n(r) dr}{\int_0^{\infty} r^3 n(r) dr} \right]}, \quad (\text{B2})$$

where  $r$  is the droplet radius,  $n(r)$  is the cloud droplet size distribution, and  $r_c$  is the critical radius for autoconversion. Liu et al. (2004) derived an analytical expression for predicting  $r_c$  in the autoconversion parameterization:

$$r_c \approx 4.09 \times 10^{-4} \beta_{con}^{1/6} \frac{N^{1/6}}{L^{1/3}}, \quad (\text{B3})$$

where  $\beta_{con} = 1.15 \times 10^{23}$  is an empirical coefficient.

### Appendix C: Relationship between Fog Liquid Water Content and Thickness

According to the asymptotic analysis through a singular perturbation method by Zhou and Ferrier (2008), the vertical distribution of liquid water content ( $L$ ) for steady radiation fog can be expressed by

$$L(z, K) = \left[ \frac{\beta(p, T_e) C_o H}{\alpha} \right]^{1/2} \left[ \left( 1 - \frac{z}{H} \right)^{1/2} - \frac{2}{1 + e^{z/\delta}} \right], \quad (\text{C1})$$

where  $\alpha$ ,  $H$ ,  $z$ ,  $K$ ,  $p$ ,  $T_e$  are gravitational settling parameter, depth of fog bank, height, turbulent exchange coefficient, air pressure and air temperature, respectively.

$\beta(p, T_e) C_o$  is the condensation rate per unit mass due to cooling of the air.

$C_o = -\partial T_e / \partial t$  (in  $\text{K sec}^{-1}$ ) is the total local cooling rate and the slope  $\beta(p, T_e)$  can

be expressed using the Clausius–Clapeyron equation as

$$\beta(p, T_e) = \frac{622 L_v e_s(T_e)}{R_v T_e^2 p}, \quad (\text{C2})$$

where  $L_v$  and  $R_v$  are the latent heat and the gas constant for vapor, respectively, and  $e_s$  is the saturation vapor pressure. The quantity  $\delta$  can be thought of as a fog boundary



layer expressed as

$$\delta = \frac{K}{2[\alpha\beta(p,T_e)C_oH]^{1/2}}. \quad (C3)$$

Setting  $K \rightarrow 0$  in (C1), the maximum possible value for the liquid water content of fog near the surface can be obtained as

$$L_{\max} = \left[ \frac{\beta(p,T_e)C_oH}{\alpha} \right]^{1/2}. \quad (C4)$$

## REFERENCES

- Beiderwieden, E., A. Schmidt, Y. J. Hsia, S. C. Chang, T. Wrzesinsky, and O. Klemm, 2007: Nutrient input through occult and wet deposition into a subtropical montane cloud forest. *Water Air Soil Pollut*, **186**, 273-288.
- Costa, A. A., C. J. de Oliveira, J. C. P. de Oliveira, and A. J. d. C. Sampaio, 2000: Microphysical observations of warm cumulus clouds in Ceará Brazil. *Atmospheric Research*, **54**(2-3), 167-199.
- Croft, P. J., R. L. Pfof, J. M. Medlin, and G. A. Johnson, 1997: Fog forecasting for the southern region: A conceptual model approach. *Weather and Forecasting*, **12**(3), 545-556.
- Eldridge, R. G., 1966: Haze and fog aerosol distributions. *J. Atmos. Sci.*, **23**, 605-613.
- Eldridge, R. G., 1971: The relationship between visibility and liquid water content in fog. *J. Atmos. Sci.*, **28**, 1183-1186.
- Eugster, W., R. Burkard, F. Holwerda, F.N. Scatena, and L.A. Bruijnzeel, 2006: Characteristics of fog and fogwater fluxes in a Puerto Rican elfin cloud forest. *Agricultural and Forest Meteorology*, **139**, 288-306.
- Fuzzi, S., and Coauthors, 1992: The Po Valley fog experiment 1989: An overview. *Tellus*, **44B**, 448-468.
- García-García, F., U. Virafuentes, and G. Montero-Martínez, 2002: Fine-scale measurements of fog-droplet concentrations: A preliminary assessment. *Atmos. Res.*, **64**, 179-189.
- Gerber, H.E., 1981: Microstructure of a radiation fog. *J. Atmos. Sci.*, **38**, 454-458.
- Gerber, H.E., 1991: Supersaturation and droplet spectral evolution in fog. *J. Atmos. Sci.*, **48**, 2569-2588.
- Guedalia, D., and T. Bergot, 1994: Numerical forecasting of radiation fog. Part II: A

- comparison of model simulation with several observed fog events. *Mon. Wea. Rev.*, **122**, 1231-1246.
- Gultepe, I., and G. A. Isaac, 2004: An analysis of cloud droplet number concentration (Nd) for climate studies: Emphasis on constant Nd. *Q. J. Royal Met. Soc.*, **130** A(602), 2377-2390.
- Gultepe, I., and J.A. Milbrandt, 2007: Microphysical observations and mesoscale model simulation of a warm fog case during FRAM project. *Pure Appl. Geophys.*, **164**, 1161-1178.
- Gultepe, I., G. A. Isaac, and K. Strawbridge, 2001: Variability of cloud microphysical and optical parameters obtained from aircraft and satellite remote sensing during RACE. *Inter. J. Climate*, **21**(4), 507-525.
- Gultepe, I., and Coauthors, 2007: Fog research: A review of past achievements and future perspectives. *Pure appl. geophys.*, **164**(6), 1121-1159.
- Gultepe, I., and Coauthors, 2009: The fog remote sensing and modeling field project. *Bulletin of the American Meteorological Society*, **90**(3), 341-359.
- Guo, X. and G. Zheng, 2009: Advances in weather modification from 1997 to 2007 in China. *Adv. Atmos. Sci.*, **26**(2), 240-252. doi: 10.1007/s00376-009-0240-8
- Herckes, P., H. Chang, T. Lee, and J. L. Jr. Collett, 2007: Air pollution processing by radiation fogs. *Water, Air, Soil Pollut.*, **181**, 65-75.
- Hong Z., and M. Huang, 1965: The second maximum and other related characteristics of the Southern Mountain cloud spectra. *The study on microphysics of cloud/fog precipitation in China*, Gu Z. Ed., Science Press, 18-29. (in Chinese)
- Hsieh, W. C., H. Jonsson, L.-P. Wang, G. Buzorius, R. C. Flagan, J. H. Seinfeld, and A. Nenes, 2009: On the representation of droplet coalescence and autoconversion: Evaluation using ambient cloud droplet size distributions, *J. Geophys. Res.*, **114**,

D07201, doi:10.1029/2008JD010502.

- Huang, Y., Y. Huang, Z. Li, B. Chen, J. Huang, and J. Gu, 2000: The microphysical structure and evolution of winter fog in Xishuangbanna. *Acta Meteorologica Sinica*, **55**(6), 715-725. (in Chinese)
- Hudson, J.G., 1980: Relationship between fog condensation nuclei and fog microstructure. *J. Atmos. Sci.*, **37**, 1854-1867.
- Hudson, J. G., and G. Svensson, 1995: Cloud microphysical relationships in California marine stratus. *J. Appl. Meteor.*, **34**(12), 2655-2666.
- Jaw, J.-J., 1966: Statistical theory of precipitation processes. *Tellus*, **18**, 722-729.
- Klemm, O., and T. Wrzesinsky, 2007: Fog deposition fluxes of water and ions to a mountainous site in Central Europe. *Tellus*, **59**, 705-714.
- Klemm, O., T. Wrzesinsky, C. Scheer, 2005: Fog water flux at a canopy top: Direct measurement versus one-dimensional model. *Atmospheric Environment*, **39**, 5375-5386.
- Kunkel, B. A., 1984: Parameterization of droplet terminal velocity and extinction coefficient in fog models. *J. Appl. Meteor.*, **23**, 34-41.
- Li, Z., 2001: Study of fog in China over the past 40 years. *Acta Meteorologica Sinica*, **59**(5), 616-624. (in Chinese)
- Li, Z., L. Zhong and X. Yu, 1992: The temporal-spatial distribution and physical structure of land fog in southwest China and the Changjiang River Basin. *Acta Geographica Sinica*, **47**(3), 242-251. (in Chinese)
- Li, Z., J. Huang, Y. Huang, Z. Yang, and Q. Wang, 1999a: Study on the physical process of winter valley fog in Xishuangbanna Region. *Acta Meteorological sinica*, **13**(4), 494-508. (in Chinese)
- Li, Z., J. Huang, Y. Zhou, and S. Zhu, 1999b: Physical structures of the five-day

- sustained fog around Nanjing in 1996. *Acta Meteorologica Sinica*, **57**(5), 622-631.  
(in Chinese)
- Liu, Y., 1992: Skewness and kurtosis of measured raindrop size distributions. *Atmospheric Environment*, **26A**, 2713-2716.
- Liu, Y., 1993: Statistical theory of the Marshall-Palmer distribution of raindrops. *Atmospheric Environment*, Part A, General Topics, **27**(1), 15-19.
- Liu, Y., and F. Liu, 1994: On the description of aerosol particle size distribution. *Atmospheric Research*, **31**(1-3), 187-198.
- Liu, Y., P.H. Daum, S.K. Chai, and F. Liu 2002: Cloud parameterizations, cloud physics, and their connections: An overview. *Recent Res. Devel. Geophysics*, **4**, 119-142.
- Liu, Y., P. H. Daum, and R. L. McGraw, 2004: An analytical expression for predicting the critical radius in the autoconversion parameterization. *Geophys. Res. Lett.*, **31**, L06121, doi:10.1029/2003GL019117.
- Liu, Y., P. H. Daum, and R. L. McGraw, 2005: Size truncation effect, threshold behavior, and a new type of autoconversion parameterization. *Geophys. Res. Lett.*, **32**, L11811, doi:10.1029/2005GL022636.
- Liu, Y., P. H. Daum, R. L. McGraw, and M. Miller, 2006: Generalized threshold function accounting for effect of relative dispersion on threshold behavior of autoconversion process. *Geophys. Res. Lett.*, **33**, L11804, doi:10.1029/2005GL025500.
- Liu, Y., L. You, W. Yang, F. Liu, 1995: On the size distribution of cloud droplets. *Atmospheric Research*, **35**(2-4), 201-216.
- Lu, C., S. Niu, J. Yang, and W. Wang, 2008: An Observational Study on Physical Mechanism and Boundary Layer Structure of Winter Advection Fog in Nanjing.

- Journal of Nanjing Institute of Meteorology*, **31**(4), 520-529. (in Chinese)
- Niu, S., C. Lu, H. Yu, L. Zhao, J. Lü, 2009: Fog research in China: an overview. *Adv. Atmos. Sci.*, doi: 10.1007/s00376-009-8174-8. (Accepted)
- Pilié, R. J., E. J. Mack, W. C. Kocmond, C. W. Rogers and W. J. Eadie, 1975: The life cycle of valley fog. Part I: Micrometeorological characteristics. *J. Appl. Meteor.*, **14**, 347-363.
- Pinnick, R.G., D.L. Hoihjelle, G. Fernandez, E.B. Stenmark, J.D. Lindberg, and G.B. Hoidale, 1978: Vertical structure in atmospheric fog and haze and its effects on visible and infrared extinction. *J. Atmos. Sci.*, **35**, 2020-2032.
- Pu, M., and S. Shen, 2001: The climatic characteristics and the main weather systems of Jiangsu fog. *Meteorological decision-making service manual of Jiangsu Province*, Pu, M., and S. Shen, Eds., China Meteorological Press, 91-95.(in Chinese)
- Roach, W.T., R. Brown, S. J. Caughey, J. A. Garland and C. J. Readings, 1976: The physics of radiation fog: I- a field study. *Quart. J. R. Met. Soc.*, **102**, 313-333.
- Tang, H., S. Fan, D. Wu, and X. Deng, 2002: Research of the Microphysical Structure and Evolution of Dense Fog over Nanling Mountain Area. *Acta Scientiarum Naturalium Universitatis Sunyatseni*, **41**(4),92-96.(in Chinese)
- Tomasi, C., and F. Tampieri, 1976: Features of the proportionality coefficient in the relationship between visibility and liquid water content in haze and fog. *Atmosphere*,**14**,61-76.
- Tong, Y., 2008: Haze phenomenon and analysis of the characteristics of its pollutants in Nanjing area. M.S. thesis, College of Applied Meteorology, Nanjing University of Information and Science, 58pp. (in Chinese)
- Twomey, S., 1977: The influence of pollution on the shortwave albedo of clouds.

*Journal of the Atmospheric Sciences*, **34**(7), 1149-1152.

Wendisch, M., and Coauthors, 1998: Drop size distribution and LWC in Po Valley

*Fog. Contr. Atmos. Phys.*, **71**, 87-100.

Wrzesinsky, T., 2003: Direct measurement and evaluation of fog deposition of water

and trace substances into a mountainous forest ecosystem. Dissertation,

Department of Biology, Chemistry and Geosciences, University of Bayreuth, 108

pp.(in Germany)

Zhou, B., and B. S. Ferrier, 2008: Asymptotic analysis of equilibrium in radiation fog.

*J. Appl. Meteorol. Clim.*, **47**,1704-1722.

## Captions

**Figure 1.** The droplet spectrometer (model FM-100, Droplet Measurement Technologies).

**Figure 2.** The temporal variations of (a) visibility ( $Vis$ ), (b) liquid water content ( $L$ ), (c) number concentration ( $N$ ), (d) average radius ( $\bar{r}$ ), (e) standard deviation ( $\sigma$ ), (f) surface temperature ( $Temp$ ). The gray lines are 5-min-average values and the black lines are based on the results of 1800s Fast Fourier Transform (FFT) smoothing of instantaneous values (1Hz) in (b)-(e). During the whole period, the microphysical data between 01:36:07 BST and 03:27:30 BST on Dec. 27<sup>th</sup> are not available because of instrumental problems.

I Formation stage (from 22:08 BST, Dec. 24 to 00:35 BST, Dec. 25)

II Ascending period of the first  $L$  oscillation during development stage (from 00:35 BST, Dec. 25-02:45 BST, Dec. 25)

III Descending period of the first  $L$  oscillation during development stage (02:45BST, Dec. 25-13:35 BST, Dec. 25)

IV Ascending period of the second  $L$  oscillation during development stage (13:35 BST, Dec. 25-00:18 BST, Dec. 26)

V Descending period of the second  $L$  oscillation during development stage (00:18 BST, Dec. 26-13:00 BST, Dec. 26)

VI Dissipation stage (from 13:00 BST, Dec.26 to 14:14 BST, Dec.27)

**Figure 3.** The temporal evolution of spectra based on 5-min-average values.

**Figure 4.** Kurtosis deviation coefficients  $C_k$  as a function of skewness deviation coefficients  $C_s$ . The color symbols represent  $C_s$  and  $C_k$  of average spectra during six stages/periods ( I -VI as defined in Figure 2) and the whole fog event; the black cycles are the 5-min-average values calculated from observations, and the solid line



represents the relationship between  $C_s$  and  $C_k$  for a gamma distribution.

**Figure 5.** Average spectra of six stages/periods ( I -VI) as defined in Figure 2 and the whole fog event.

**Figure 6.** (a) Average radius ( $\bar{r}$ ) as a function of number concentration ( $N$ ) and (b)  $N$  as a function of liquid water content ( $L$ ) during the whole fog event.

**Figure 7.** (a) Standard deviation ( $\sigma$ ) of fog spectra as a function of average radius ( $\bar{r}$ ), (b)  $\sigma$  as a function of number concentration ( $N$ ), and (c)  $\sigma$  as a function of liquid water content ( $L$ ) during the whole fog event.

**Figure 8.** Same to Figure 2, except for the temporal variation of threshold function ( $T$ ).

**Figure 9.** (a) Average radius ( $\bar{r}$ ) as a function of number concentration ( $N$ ), (b)  $N$  as a function of liquid water content ( $L$ ), (c) standard deviation ( $\sigma$ ) as a function of  $\bar{r}$ , (d)  $\sigma$  as a function of  $N$ , (e)  $\sigma$  as a function of  $L$  and (f)  $L$  as a function of  $\bar{r}$  with different  $T$  ranges.

**Figure 10.** Average radius ( $\bar{r}$ ) as a function of number concentration ( $N$ ) during different stages/periods ( I -VI) as defined in Figure 2.

**Figure 11.** Number concentration ( $N$ ) as a function of liquid water content ( $L$ ) during different stages/periods ( I -VI) as defined in Figure 2.

**Figure 12.** Standard deviation ( $\sigma$ ) of fog spectra as a function of average radius ( $\bar{r}$ ) during different stages/periods ( I -VI) as defined in Figure 2.

**Figure 13.** Standard deviation ( $\sigma$ ) of fog spectra as a function of number concentration ( $N$ ) during different stages/periods ( I -VI) as defined in Figure 2.

**Figure 14.** Standard deviation ( $\sigma$ ) of fog spectra as a function of liquid water content ( $L$ ) during different stages/periods ( I -VI) as defined in Figure 2.

**Figure 15.** The temporal evolutions of small droplet (radius  $\leq 10\mu\text{m}$ ) and big droplet

(radius>10 $\mu$ m) number concentrations in this fog event.

**Figure 16.** Height-time cross sections of (a) wind speed ( $\text{m s}^{-1}$ ), (b) temperature ( $^{\circ}\text{C}$ ), (c) relative humidity (%), and (d) specific humidity ( $\text{g kg}^{-1}$ ) during this fog event.

**Figure 17.** Average spectra with different threshold function ( $T$ ) ranges.

**Table 1.** Means and standard deviations (in parenthesis) of key microphysical properties during different stages/periods and the whole fog event

Microphysical variables	I	II	III	IV	V	VI	The whole event
Liquid water content $L$ (g m <sup>-3</sup> )	0.001 (0.001)	0.285 (0.158)	0.283 (0.141)	0.297 (0.177)	0.206 (0.172)	0.013 (0.022)	0.158 (0.178)
Concentration $N$ (cm <sup>-3</sup> )	8.7 (12.8)	426.8 (140.2)	341.4 (87.3)	484.4 (123.0)	256.1 (99.2)	78.4 (83.7)	240.1 (185.0)
Average radius $\bar{r}$ (μm)	1.9 (0.1)	3.6 (0.7)	3.4 (0.5)	3.2 (0.5)	3.0 (0.4)	1.9 (0.3)	2.7 (0.8)
Spectra standard deviation ( $\sigma$ )	0.8 (0.1)	2.4 (0.7)	2.8 (0.6)	2.3 (0.6)	2.6 (0.6)	1.0 (0.5)	1.9 (1.0)
Maximum radius $r_{max}$ (μm)	4.0 (0.5)	14.5 (3.4)	19.0 (1.9)	18.9 (3.0)	19.6 (2.7)	8.9 (4.5)	14.5 (6.4)
Peak radius $r_p$ (μm)	1.4 (2.5×10 <sup>-2</sup> )	1.4 (1.8×10 <sup>-2</sup> )	1.4 (2.0×10 <sup>-3</sup> )	1.4 (1.3×10 <sup>-3</sup> )	1.4 (1.1×10 <sup>-3</sup> )	1.4 (1.0×10 <sup>-3</sup> )	1.4 (9.8×10 <sup>-3</sup> )

I Formation stage (from 22:08 BST, Dec. 24 to 00:35 BST, Dec. 25)

II Ascending period of the first  $L$  oscillation during development stage (from 00:35 BST, Dec. 25-02:45 BST, Dec. 25)

III Descending period of the first  $L$  oscillation during development stage (02:45BST, Dec. 25-13:35 BST, Dec. 25)

IV Ascending period of the second  $L$  oscillation during development stage (13:35 BST, Dec. 25-00:18 BST, Dec. 26)

V Descending period of the second  $L$  oscillation during development stage (00:18 BST, Dec. 26-13:00 BST, Dec. 26)

VI Dissipation stage (from 13:00 BST, Dec.26 to 14:14 BST, Dec.27)

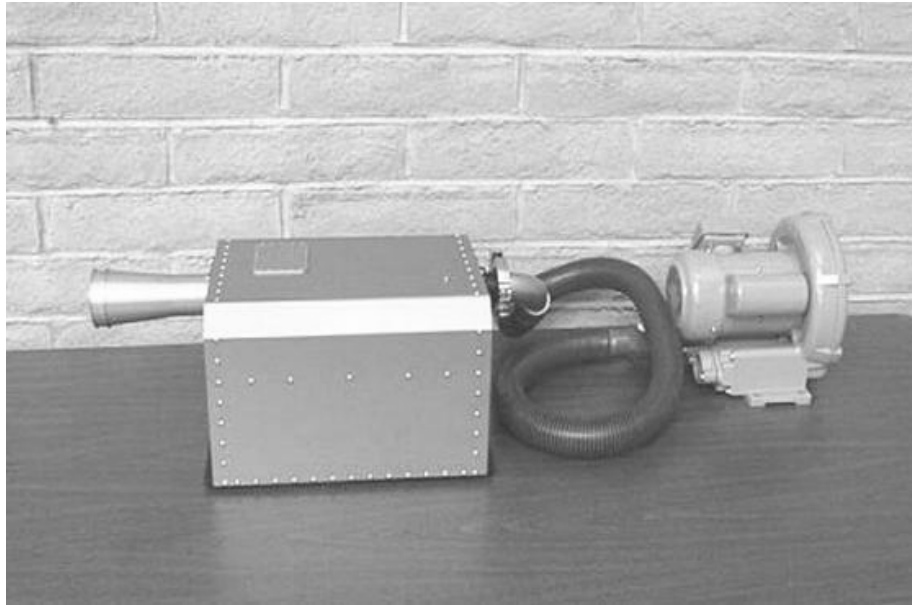


**Figure 1.** The droplet spectrometer (model FM-100, Droplet Measurement Technologies).

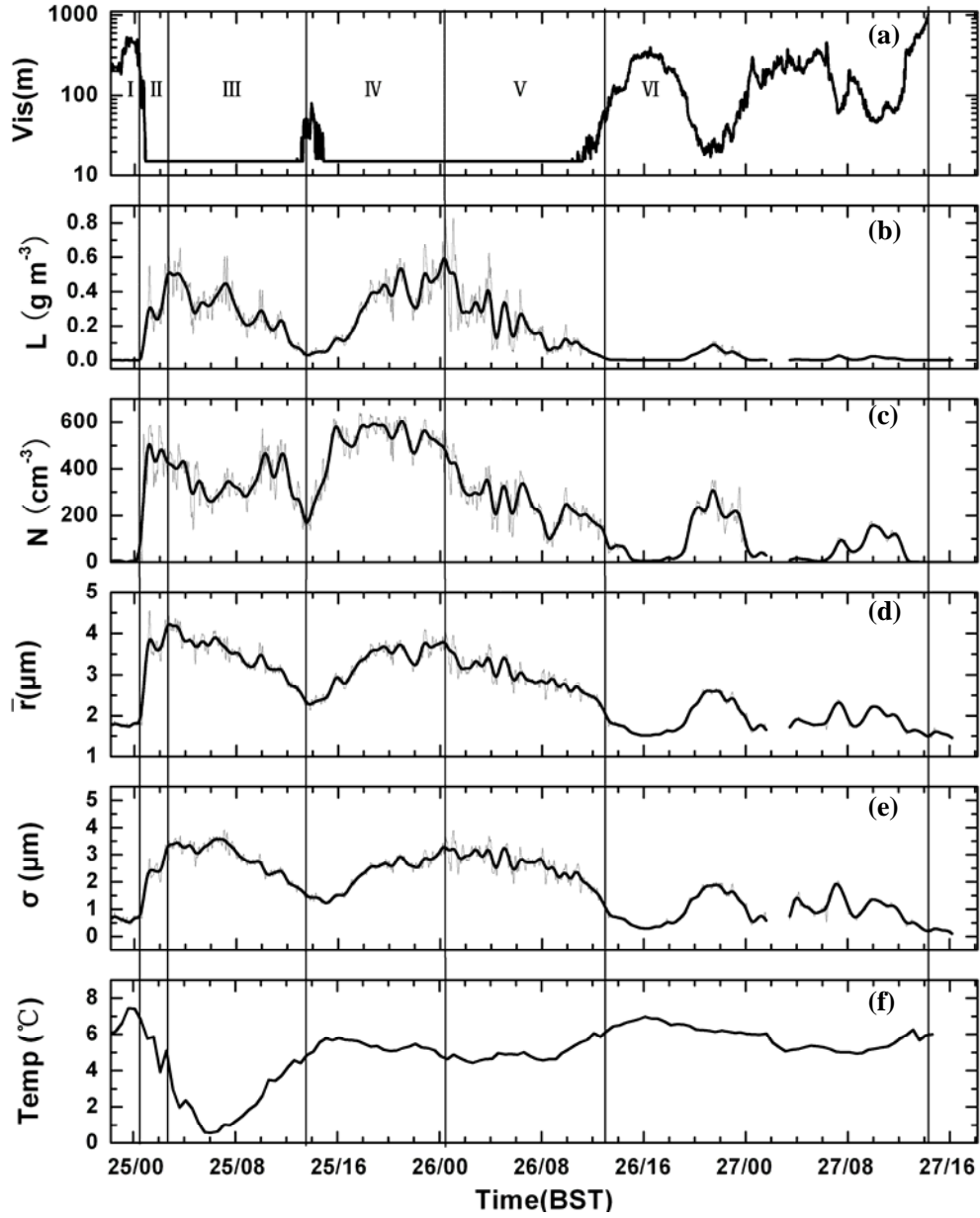


**Figure 2.** The temporal variations of (a) visibility ( $Vis$ ), (b) liquid water content ( $L$ ), (c) number concentration ( $N$ ), (d) average radius ( $\bar{r}$ ), (e) standard deviation ( $\sigma$ ), (f) surface temperature ( $Temp$ ). The gray lines are 5-min-average values and the black lines are based on the results of 1800s Fast Fourier Transform (FFT) smoothing of instantaneous values (1Hz) in (b)-(e). During the whole period, the microphysical data between 01:36:07 BST and 03:27:30 BST on Dec. 27<sup>th</sup> are not available because of instrumental problems.

I Formation stage (from 22:08 BST, Dec. 24 to 00:35 BST, Dec. 25)

- II Ascending period of the first  $L$  oscillation during development stage (from 00:35 BST, Dec. 25-02:45 BST, Dec. 25)
- III Descending period of the first  $L$  oscillation during development stage (02:45BST, Dec. 25-13:35 BST, Dec. 25)
- IV Ascending period of the second  $L$  oscillation during development stage (13:35 BST, Dec. 25-00:18 BST, Dec. 26)
- V Descending period of the second  $L$  oscillation during development stage (00:18 BST, Dec. 26-13:00 BST, Dec. 26)
- VI Dissipation stage (from 13:00 BST, Dec.26 to 14:14 BST, Dec.27)

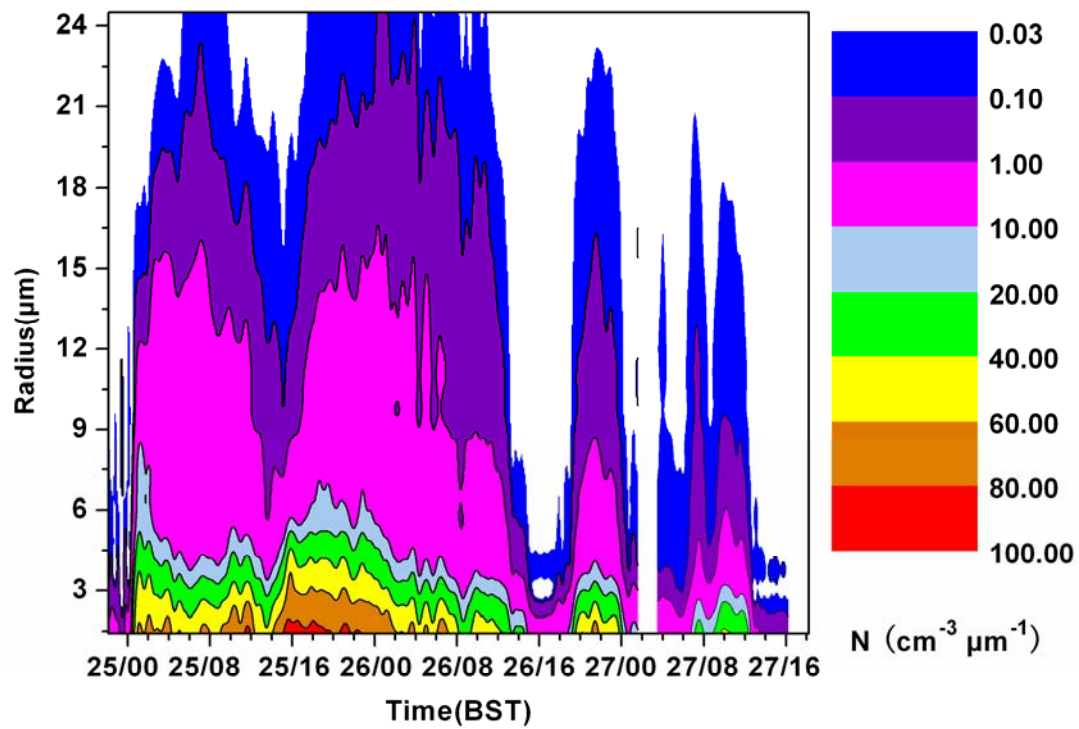


**Figure 3.** The temporal evolution of spectra based on 5-min-average values.

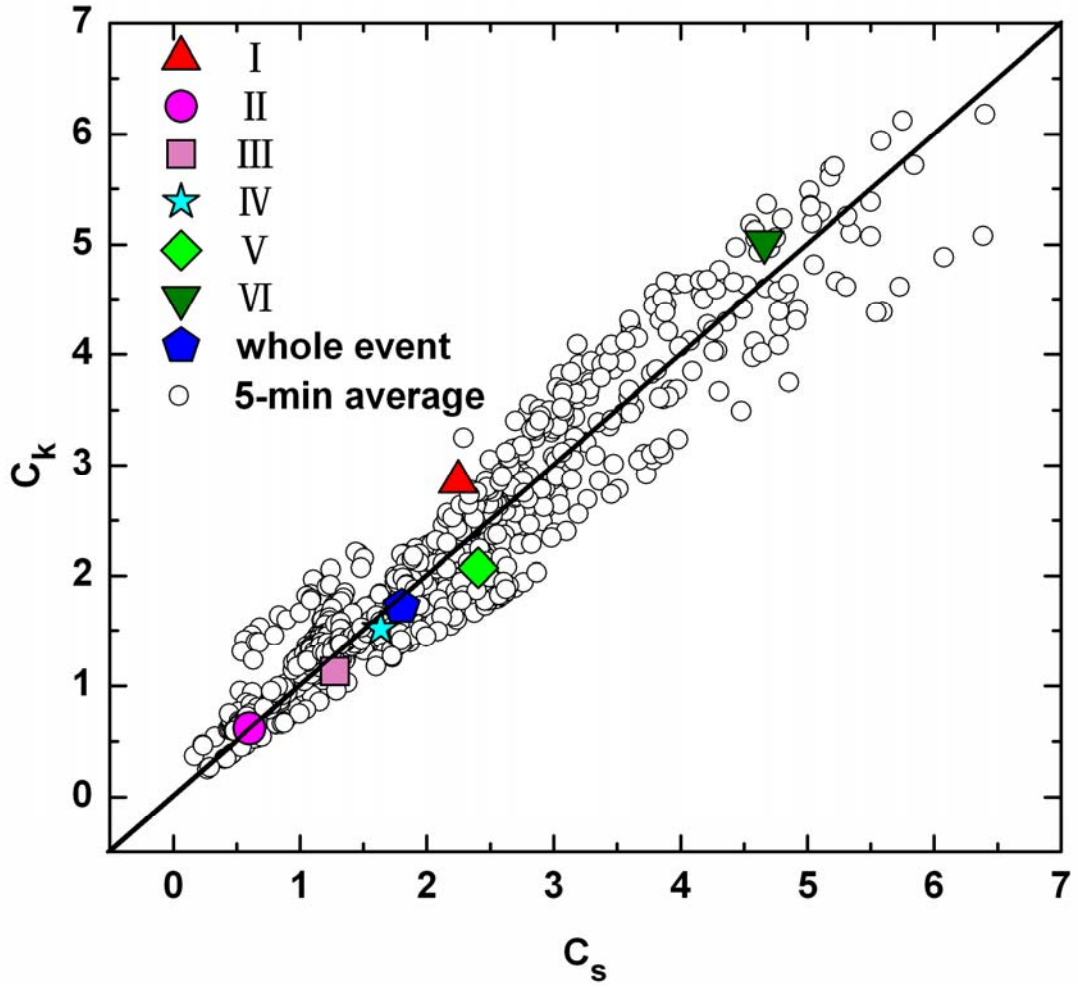


**Figure 4.** Kurtosis deviation coefficients  $C_k$  as a function of skewness deviation coefficients  $C_s$ . The color symbols represent  $C_s$  and  $C_k$  of average spectra during six stages/periods ( I -VI as defined in Figure 2) and the whole fog event; the black cycles are the 5-min-average values calculated from observations, and the solid line represents the relationship between  $C_s$  and  $C_k$  for a gamma distribution.



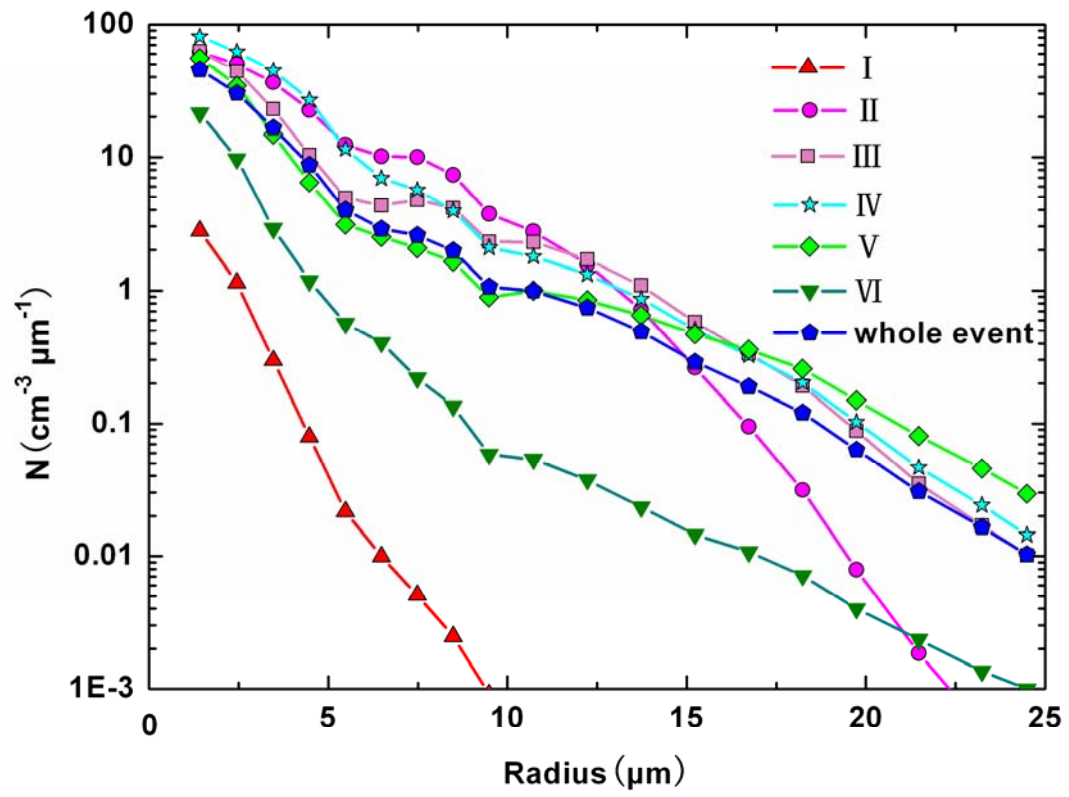


**Figure 5.** Average spectra of six stages/periods ( I -VI) as defined in Figure 2 and the whole fog event.

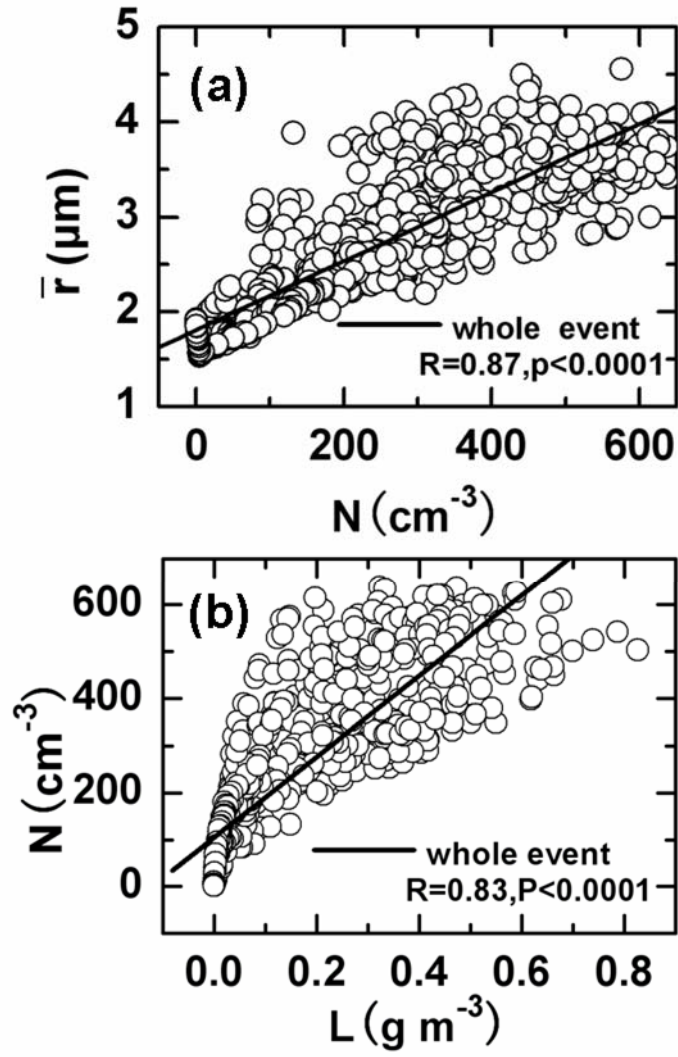


**Figure 6.** (a) Average radius ( $\bar{r}$ ) as a function of number concentration ( $N$ ) and (b)  $N$  as a function of liquid water content ( $L$ ) during the whole fog event.

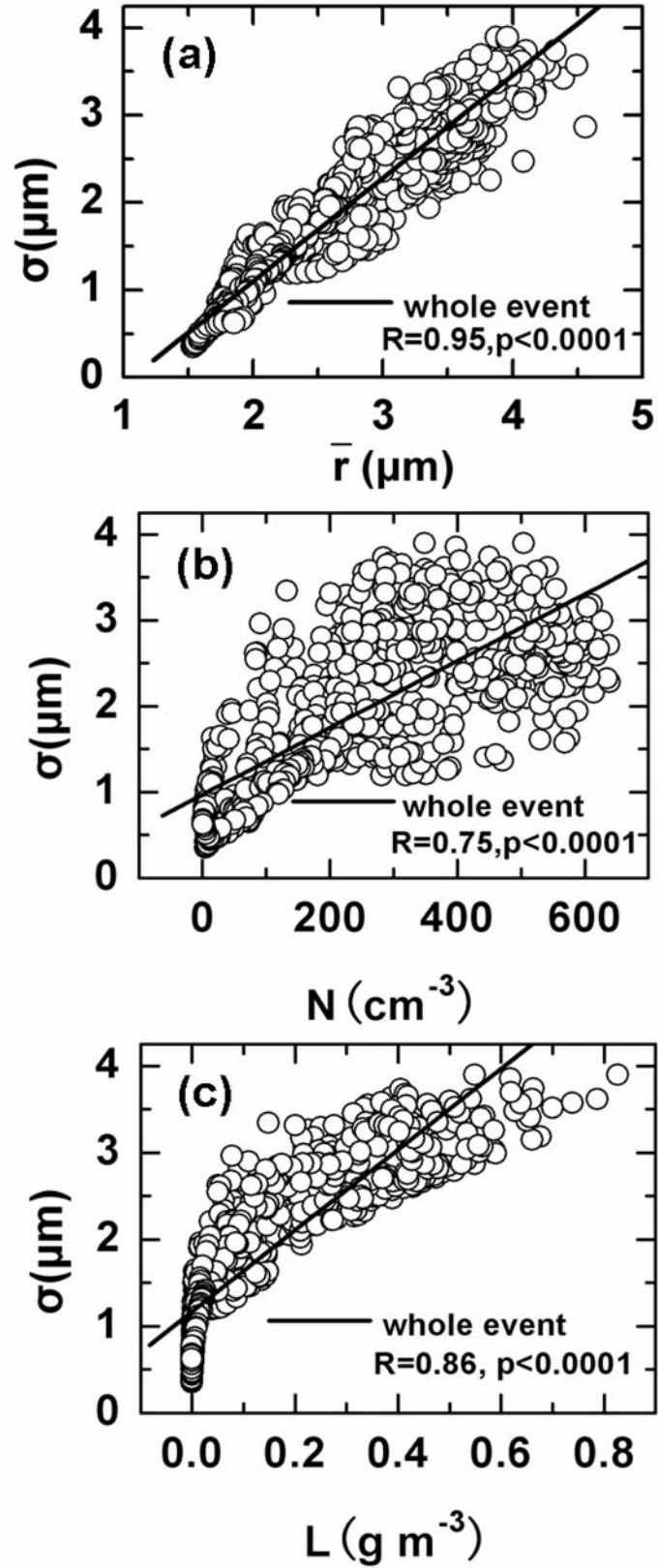


**Figure 7.** (a) Standard deviation ( $\sigma$ ) of fog spectra as a function of average radius ( $\bar{r}$ ), (b)  $\sigma$  as a function of number concentration ( $N$ ), and (c)  $\sigma$  as a function of liquid water content ( $L$ ) during the whole fog event.

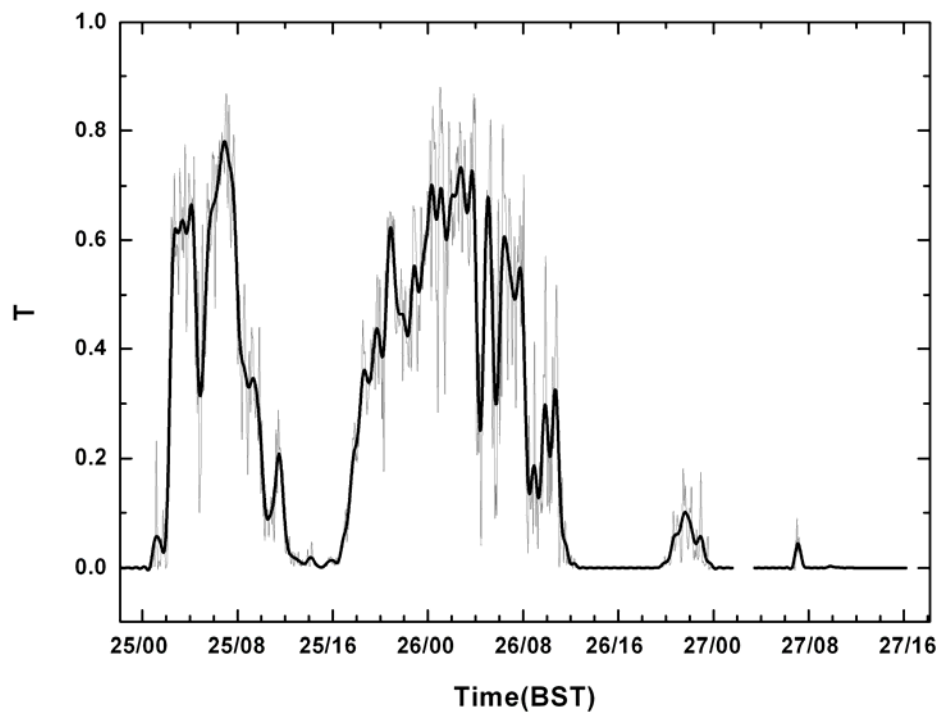


**Figure 8.** Same to Figure 2, except for the temporal variation of threshold function ( $T$ ).

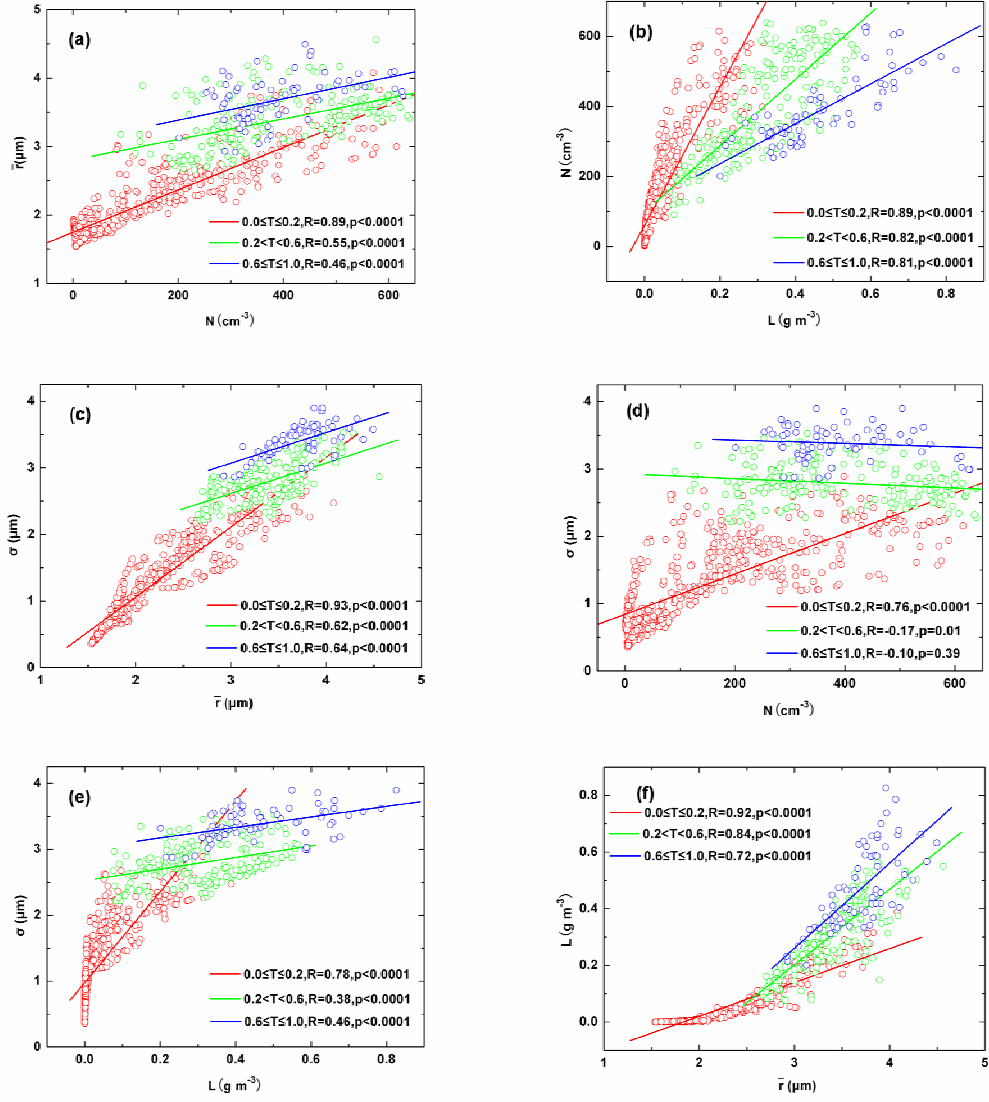


**Figure 9.** (a) Average radius ( $\bar{r}$ ) as a function of number concentration ( $N$ ), (b)  $N$  as a function of liquid water content ( $L$ ), (c) standard deviation ( $\sigma$ ) as a function of  $\bar{r}$ , (d)  $\sigma$  as a function of  $N$ , (e)  $\sigma$  as a function of  $L$  and (f)  $L$  as a function of  $\bar{r}$  with different  $T$  ranges.

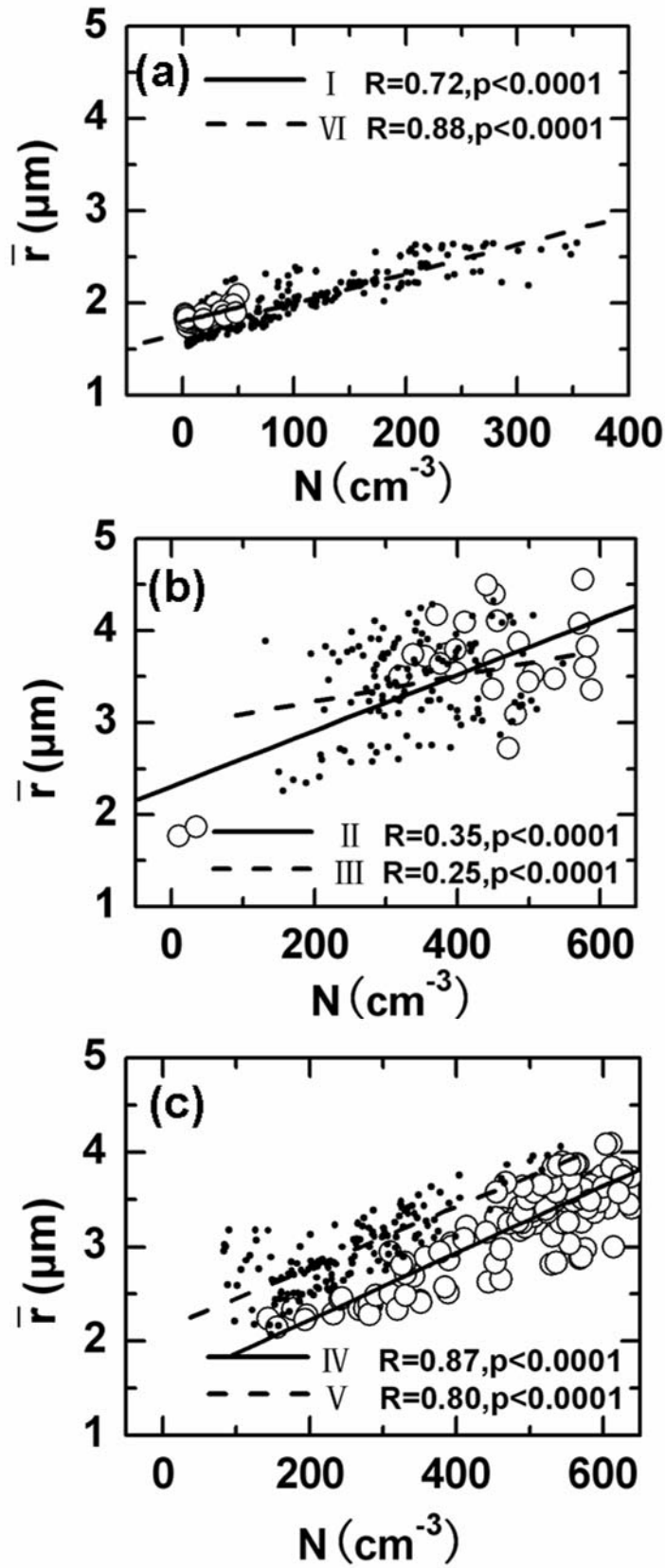


**Figure 10.** Average radius ( $\bar{r}$ ) as a function of number concentration ( $N$ ) during different stages/periods ( I -VI) as defined in Figure 2.

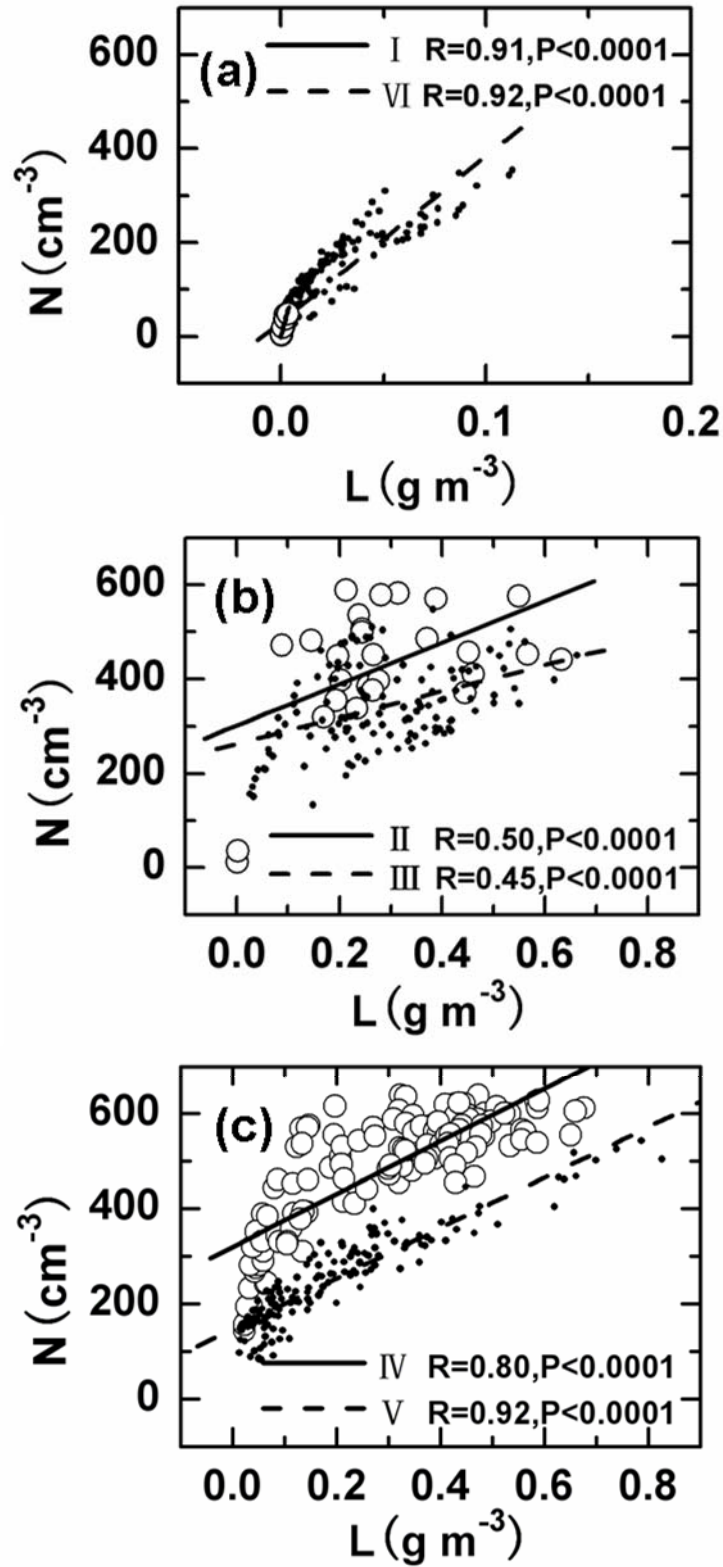


**Figure 11.** Number concentration ( $N$ ) as a function of liquid water content ( $L$ ) during different stages/periods ( I -VI) as defined in Figure 2.

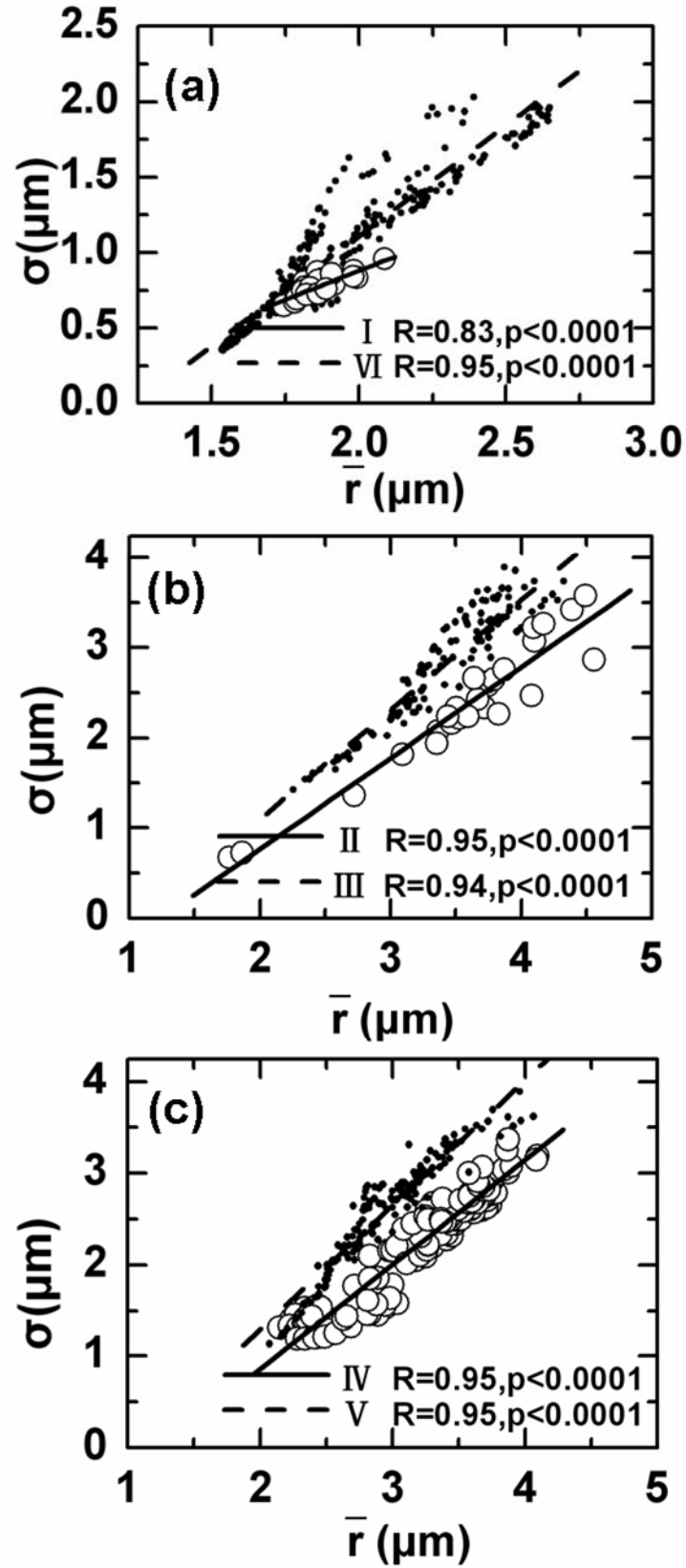


**Figure 12.** Standard deviation ( $\sigma$ ) of fog spectra as a function of average radius ( $\bar{r}$ ) during different stages/periods ( I -VI) as defined in Figure 2.



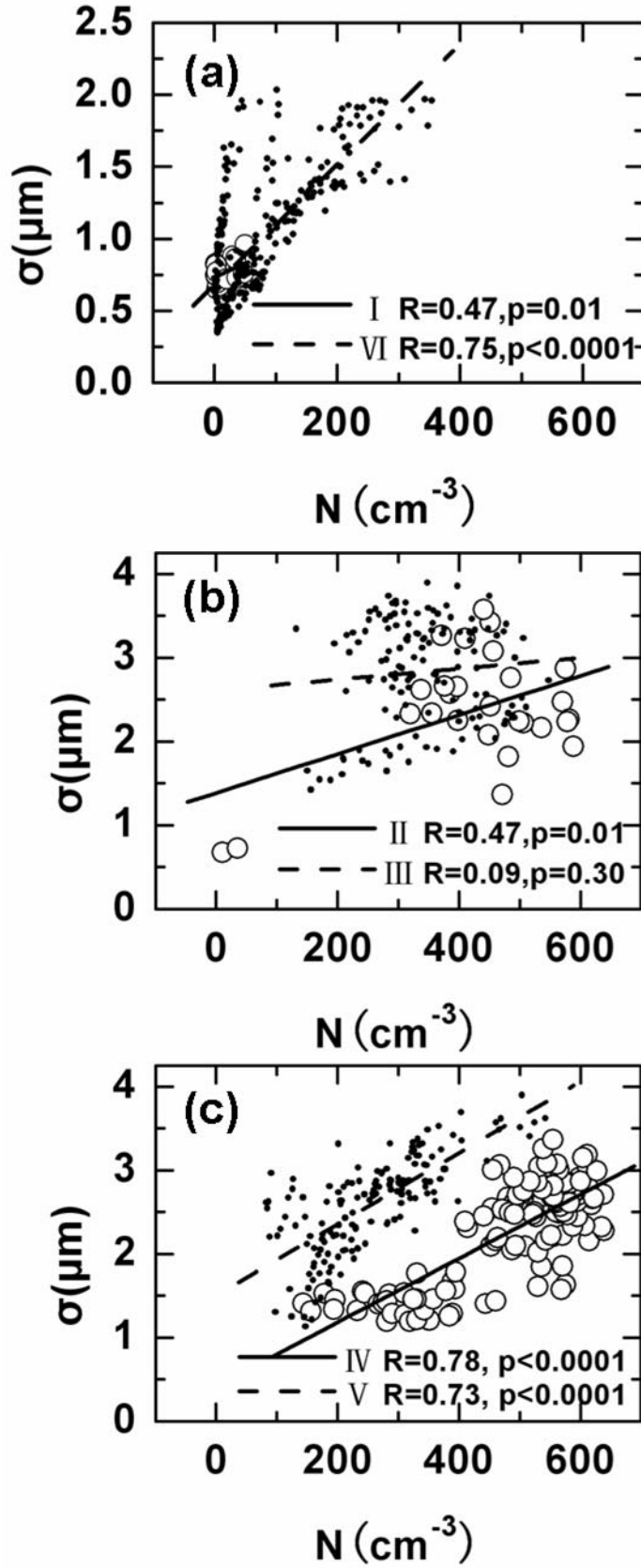


**Figure 13.** Standard deviation ( $\sigma$ ) of fog spectra as a function of number concentration ( $N$ ) during different stages/periods ( I -VI) as defined in Figure 2.

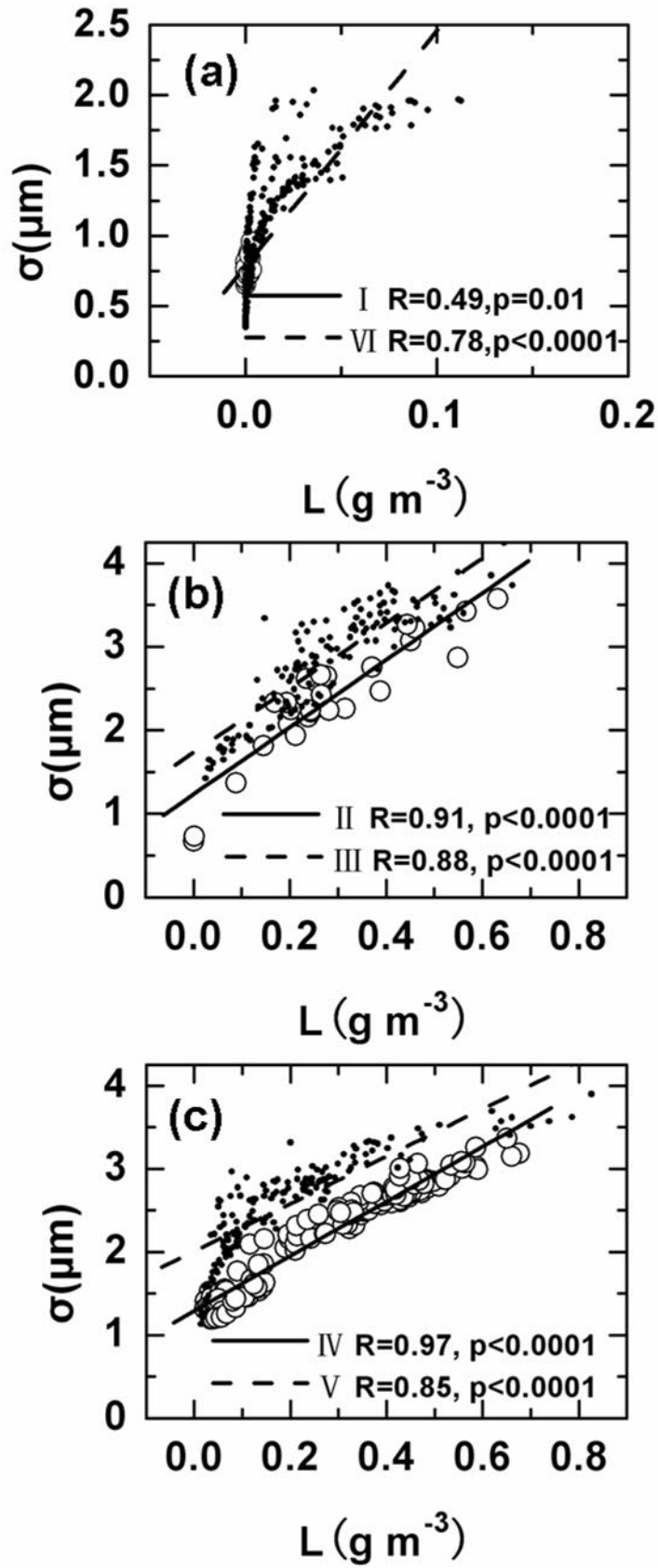


**Figure 14.** Standard deviation ( $\sigma$ ) of fog spectra as a function of liquid water content ( $L$ ) during different stages/periods ( I -VI) as defined in Figure 2.

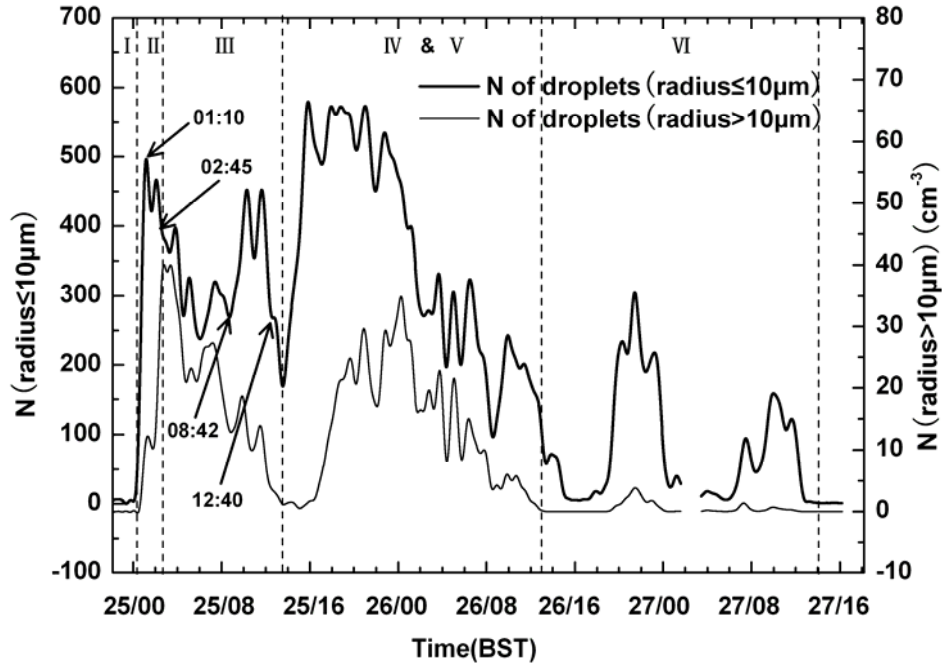


**Figure 15.** The temporal evolutions of small droplet (radius  $\leq 10\mu\text{m}$ ) and big droplet (radius  $> 10\mu\text{m}$ ) number concentrations in this fog event.

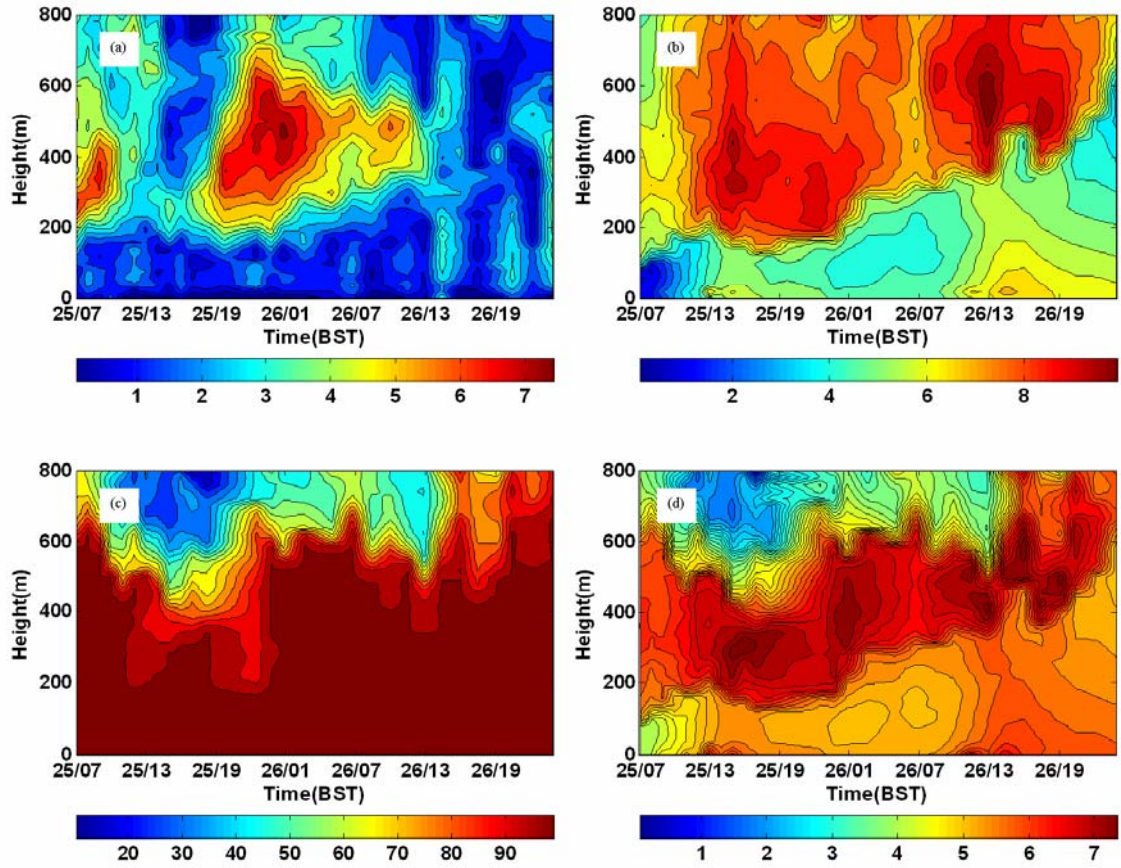


**Figure 16.** Height-time cross sections of (a) wind speed ( $\text{m s}^{-1}$ ), (b) temperature ( $^{\circ}\text{C}$ ), (c) relative humidity (%), and (d) specific humidity ( $\text{g kg}^{-1}$ ) during this fog event.

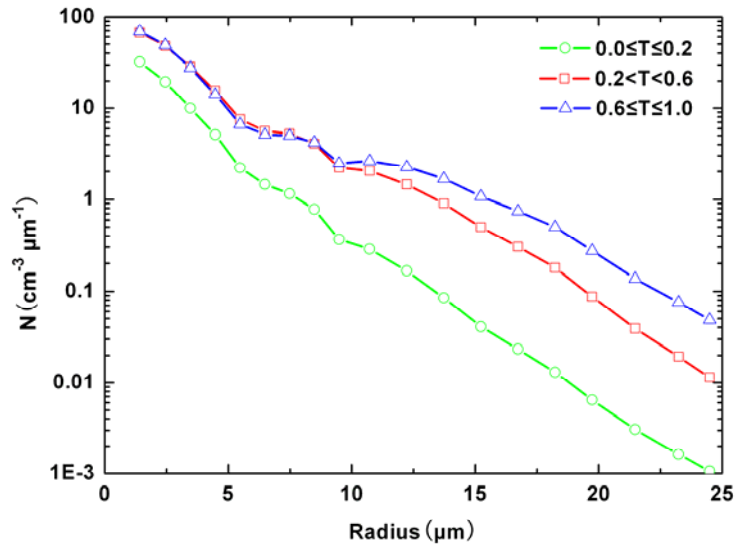


**Figure 17.** Average spectra with different threshold function ( $T$ ) ranges.